THE $^{26g}Al(p,\gamma)^{27}Si$ REACTION AT DRAGON

Heather L. Crawford[a]

[a]*TRIUMF, 4004 Wesbrook Mall, Vancouver, B.C., Canada, V6T 2A3*

ABSTRACT

The astrophysically important $^{26g}Al(p,\gamma)^{27}Si$ radiative proton capture reaction was recently investigated using the ISAC-DRAGON facility at TRIUMF. In this experiment, an intense radioactive ^{26g}Al beam produced at the ISAC radioactive beam facility was used in conjunction with a windowless H_2 gas target at the DRAGON facility to investigate narrow resonances which are believed to dominate the rate of this reaction in explosive stellar environments such as novae and supernovae explosions. The 188 keV resonance in ^{27}Si was investigated over a 3 week running period, during which approximately 250 runs were taken. From the data collected, the thick target yield of the reaction will be determined, which will then be used to calculate an experimental value for the resonance strength, a value that can be used in astrophysical models attempting to describe the reactions occurring in explosive stellar nucleosynthesis. The purpose of this project was to work on determining two quantities critical to the calculation of the thick target yield and resonance strength: the normalized beam particles on target over the run, and the BGO gamma array detection efficiency. Two methods of beam normalization were used and refined in the analysis of the experimental runs, and validated one another, showing agreement within 8%. BGO efficiency was evaluated using GEANT simulations for a number of different angular distributions and thresholds, to provide averaged efficiency values. Further work on incorporating angular distributions of emitted gamma radiation into the GEANT simulation is ongoing, and will improve the accuracy of efficiency calculations.

CONTENTS

LIST OF FIGURES

LIST OF TABLES

1 INTRODUCTION

1.1 STELLAR LIFECYCLE AND NUCLEOSYNTHESIS

Stars are the factories of the cosmos; it is in these giant burning spheres that most of the chemical elements above hydrogen are first produced. Whether in the relative calm of normal burning cycles or in the violent heat and pressure of an exploding star, all of the chemical elements that make up our world are formed by nuclear reactions that have been occurring for billions of years and continue in the heavens today.

Within the first three minutes after the Big Bang hydrogen nuclei fused to form helium, and very small amounts of lithium and beryllium. However, all nucleosynthesis past that point occurs within stars, or during their violent explosive deaths [1]. Stars are born within nebulae, massive clouds of mainly hydrogen gas, which collapse under the force of gravity, increasing the pressure and temperature of the gas until such a point when the gravitational force is balanced by the internal thermal energy within the star. During this time, the temperature at the center of the star increases until it reaches around 10^7 K and nuclear reactions can begin to occur. In the longest, main burning stage, accounting for the bulk of a stars lifetime, hydrogen nuclei are brought together in a series of reactions to form helium, a process known as hydrogen burning. During this time, the star is known as a main-sequence star. Once the hydrogen fuel in the stellar core is exhausted, this burning stage ends and the stellar core rapidly begins to collapse once again, heating to approximately 10^8 K until helium burning is ignited, a process which results in the production of carbon and oxygen. During this collapse and heating of the core, the outer stellar layers actually expand and cool, giving the star a redder appearance, as it becomes a red giant. What happens next depends on the mass of the star. Very massive stars (>8 $M_\odot$) continue the cycle of collapsing and heating, igniting new nuclear burning cycles with each step, eventually forming elements up to the iron group. However, when nuclear fuel finally runs out and fusion no longer yields energy, the massive stellar core, composed almost entirely of iron (whose fusion requires energy, rather than releasing it), rapidly collapses and heats, resulting in a massive supernova explosion, in which rapid neutron and proton captures allow the formation of elements up to the uranium region, in the r- and rp-processes which occur faster than the competing beta decays of the radioactive intermediate species. In this process the star is either completely destroyed, or leaves behind an extremely high-density core, in the form of a black hole or a neutron star. This situation describes a Type II supernova, the most common type of supernova explosion. Alternatively, small stars with masses in the range of 1-1.4 $M_\odot$, experience

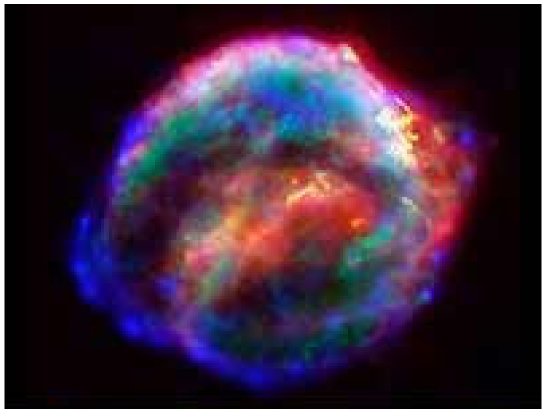

FIGURE 1.1: *The expanding remains of Kepler's supernova – SN 1604 – a composite view composed of ultraviolet, infrared and visible light components* [2].

continued condensing of the core, with expansion and cooling of the outer layers. Eventually the outer hydrogen rich envelope is ejected, and forms a new nebula, while the core becomes a white dwarf, a burned out stellar cinder, formed mainly of carbon and oxygen, and stabilized against further collapse by the degenerate pressures of the electron gas. However, a white dwarf can still be rejuvenated and further participate in nucleosynthesis.

Novae explosions, a different phenomenon from supernovae, which do not involve the stellar core, are believed to be the result of the thermonuclear runaway on the surface of a white dwarf within a binary star system. A younger companion star accretes its outer layers of hydrogen rich material onto the surface of the white dwarf, where it mixes with the carbon and oxygen rich outer layers of the white dwarf, which provide a spark, and power the nova explosion through rapid radiative proton captures, once nuclear reactions are ignited. As with a supernova, within a nova explosion, the high temperatures and pressures allow these radiative capture reactions to proceed faster than the competing beta decays of the reactive radioactive nuclei, forming nuclei that could not be formed in standard burning stages.

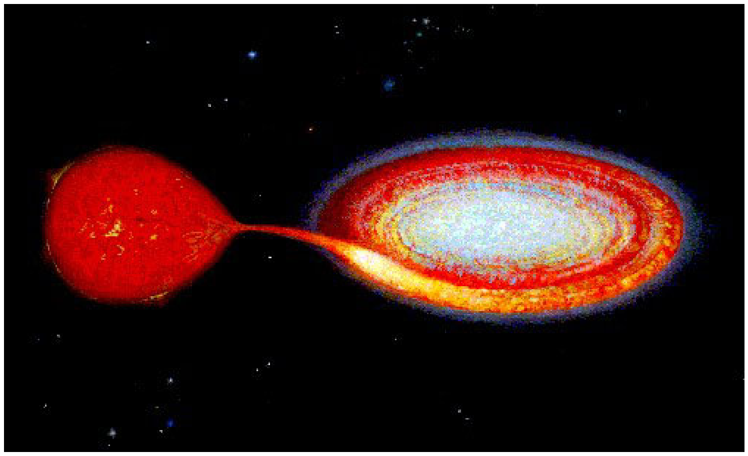

FIGURE 1.2*: Artist's impression of a binary system, and the accretion disk onto a white dwarf.*

1.2 ASTROPHYSICAL IMPORTANCE OF THE $^{26g}Al(p,\gamma)^{27}Si$ REACTION

The $^{26g}Al(p,\gamma)^{27}Si$ reaction, diagrammatically illustrated in figure 1.3, is one of the reactions involving a radioactive species that is believed to occur in novae and supernovae explosions. In these explosive environments the radiative proton capture reaction occurs more rapidly than the beta decay of ^{26g}Al, and thus this reaction has a significant and direct impact on the abundance of ^{26g}Al, a relatively long-lived radioactive nucleus which is produced as a part of the Mg-Al cycle, given below and shown graphically within figure 1.4.

$$^{24}Mg(p,\gamma)^{25}Al(\beta^{+})^{25}Mg(p,\gamma)^{26}Al$$

As the only direct method of destruction of ^{26g}Al aside from its beta decay, the $^{26g}Al(p,\gamma)$ reaction is critical when investigating the abundance of ^{26g}Al, which is in a relatively unique position for investigation [3]. ^{26g}Al undergoes positron decay (with a half-life of 717,000 years) to the first excited state of ^{26}Mg which immediately decays with a characteristic 1.809 MeV gamma ray, meaning that ^{26g}Al can be directly observed by orbiting gamma telescopes. Direct observations of abundances allow comparison with calculated values from network calculations and models attempting to describe novae and supernovae explosions. The relevant reaction rates are important parameters within these models, and these rates, including that of the $^{26g}Al(p,\gamma)^{27}Si$ reaction, must be determined experimentally.

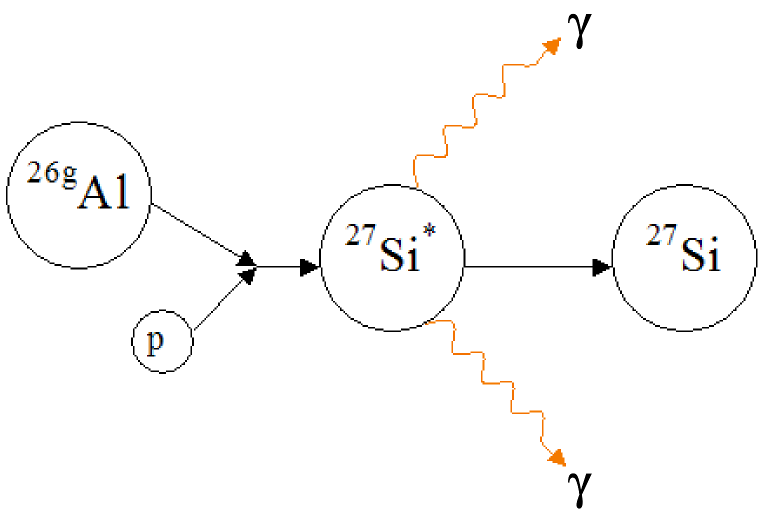

FIGURE 1.3: *A schematic representation of the ^{26g}Al(p,γ)^{27}Si reaction – a proton is captured by a ground state ^{26}Al nucleus, forming ^{27}Si and one or more gamma rays.*

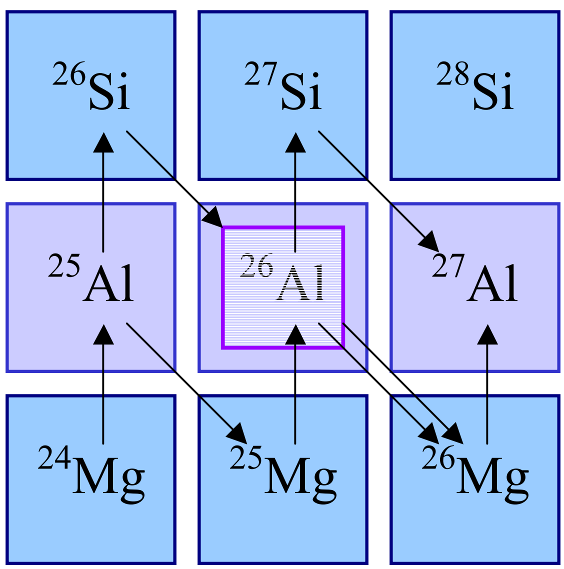

FIGURE 1.4: *A schematic representation of the Mg-Al system, showing all reactions affecting the abundance of ^{26g}Al. All vertical arrows represent (p,γ) radiative capture reactions, while downward slanted arrows represent positron decays. ^{26g}Al is produced by the ^{25}Mg(p,γ) reaction, and is destroyed through its beta decay and the ^{26g}Al(p,γ) reaction to ^{27}Si. The abundance of ^{26g}Al is also affected by the ^{25}Al(p,γ) reaction which removes ^{25}Al from the Mg-Al cycle to form ^{26}Si, which decays to ^{26m}Al, which bypasses ^{26g}Al as it decays to ^{26}Mg.*

1.3 Reaction Rates and Resonance Strength

Even at the extreme temperatures within stars during their burning stages and or during a nova or super-nova explosion, most nuclear reactions are blocked by the Coulomb barrier, an electrostatic barrier created due to the repulsive interaction between a positively charged nucleus and a positively charged incoming particle, given by the following equation:

$$V_C = \frac{1}{4\pi\varepsilon_o} \frac{Z_1 Z_2 e^2}{(R_1 + R_2)} \tag{1.1}$$

Despite the high temperatures reactant nuclei simply do not have enough energy to overcome this barrier, and must find another way to react. It is for this reason that most stellar nuclear reactions are sub-barrier, and involve penetration of the Coulomb barrier. However, the probability distribution for tunneling through the Coulomb barrier at energies typical in stars is very low, and in fact this distribution only overlaps with the extremely high-energy tail of the Maxwell-Boltzmann distribution of thermal velocities in a star. Within the overlap region both of these distributions take on very small values, but their convolution leads to a peak, known as the Gamow peak, within which there is a sufficiently high probability for reaction such that reactions occur at a significant rate [1]. This is shown graphically in figure 1.5.

While non-resonant reactions can and do occur at reasonable rates within stars, reaction rates are greatly enhanced, often dominated, by the presence of a resonance, or a stable state in the daughter nuclide within the range of stellar energies. The reaction rate of the ^{26g}Al(p,γ)^{27}Si reaction, like most nuclear reactions, is believed to be largely dominated by a few narrow resonances, which occur within the range of energies found in explosive stellar environments.

The cross-section for a single narrow resonant reaction [1] of the form X(a,b)Y is given by the Breit-Wigner formula:

$$\sigma(a,b) = \frac{2J_r + 1}{(2J_X + 1)(2J_a + 1)} (1 + \delta_{12}) \pi \lambda\!\!\!^{-}{}^2 \frac{\Gamma_a \Gamma_b}{(E - E_R)^2 + (\Gamma/2)^2} \tag{1.2}$$

where $J_r = J_X + J_a + \ell_a$ is a statistical factor depending on the spins of the particles involved, and the angular momentum of the interaction, $\Gamma_{a/b}$ refer to the level widths of the initial and final states, Γ refers to the total level width ($\Gamma_a + \Gamma_b$) and E_R is the resonance energy.

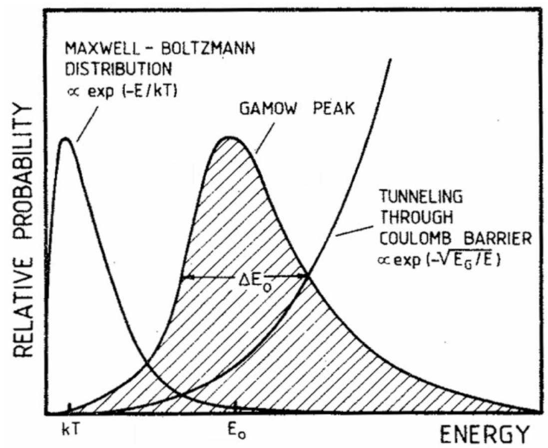

FIGURE 1.5: *A graphical representation of the overlap between the high energy tail of the Maxwell-Boltzmann thermal velocity distribution and the low probability tail of penetration through the Coulomb barrier, forming the Gamow peak of reactivity.*

This cross-section can be re-arranged slightly and combined into the general equation for the stellar reaction rate (not presented here) to give the following stellar reaction rate per particle pair for a single narrow resonance [1]:

$$< \sigma \upsilon > = \left(\frac{2\pi}{\mu kT} \right) h^2 \omega\gamma \exp\left(-\frac{E_R}{kT} \right) \tag{1.3}$$

where μ is the reduced mass of the system, T is the temperature within the stellar environment, $\omega = \frac{2J_R + 1}{(2J_X + 1)(2J_a + 1)}$ is the statistical spin factor, and $\gamma = \frac{\Gamma_a \Gamma_b}{\Gamma}$. It becomes clear that the stellar reaction rate for a narrow resonance reaction depends on the temperature within the star (T), the resonance energy (E_R), and the factor ωγ, which is known as the resonance strength. If a state has more than one narrow resonance, the stellar reaction rate is taken simply to be as above with ωγ replaced by the sum of all resonance strengths.

1.4 THICK TARGET YIELD

As was mentioned previously, knowledge of the stellar reaction rate at various temperatures requires knowledge of the resonance strength, denoted by ωγ. One method of determining this resonance strength is to experimentally measure the thick target yield [1] for a reaction, which is given by the following equation:

$$Yield = \frac{\lambda^2}{2} \frac{1}{\varepsilon} \left(\frac{M + m}{M} \right) \omega\gamma \tag{1.4}$$

where ε is the stopping power of the target material, m and M are the masses of the target and projectile nuclei respectively and once again, ωγ is the resonance strength for the reaction. Since the thick target yield, or the yield per incoming particle, can be experimentally determined, as can ε, and the masses of the nuclei are well known, resonance strength can be experimentally determined from an experiment measuring thick target yield.

While this sounds relatively straight forward, determination of the thick target yield requires accurate knowledge of a number of critical quantities: the number of recoils detected, and the number of beam particles incident on the target, as well as the efficiency of the BGO array used for detection of gamma rays and the fraction of the recoils in the charge state used within the experiment, as shown in by the following equation for thick target yield:

$$Yield = \frac{\#\mathrm{Re}coils}{(\#BeamParticles)\times(Ch\arg eStateFraction)\times(BGOEfficiency)} \tag{1.5}$$

Recoils are detected in the DRAGON system (to be discussed further in the following section) using γ-heavy ion coincidence detection, which involves the detection of a prompt reaction gamma ray at the BGO array surrounding the gas target, followed by a heavy ion signal at the end detector after a certain amount of time, determined by knowing the time of flight of a recoil from the gas target through the separator to the end detector. While determination of the number of events is not the purpose of this report, it can be said that 11 recoils, or true events, were detected during the experiment.

Determination of the number of incident beam particles on target over the course of the experiment is the focus of the remainder of this paper and will be discussed at length in the following sections.

Determination of the BGO efficiency will also be discussed as part of this paper, while an accurate measurement of the charge state of the recoils is still to be done.

1.5 DRAGON FACILITY

The DRAGON, or Detector of Recoils And Gammas Of Nuclear reactions [4], at TRIUMF is a mass-separator used in the study of astrophysical radiative capture (p,γ or α,γ) reactions. A schematic diagram of this system is shown in figure 1.6. Working in conjunction with the ISAC radioactive beam facility, DRAGON is used to separate the products of a nuclear reaction, referred to henceforth as recoils, from the bulk of the radioactive beam used in the reaction. DRAGON consists of three major components: a windowless gas target surrounded by a BGO γ-array, a two-stage electromagnetic separator and a final heavy-ion detector. An intense

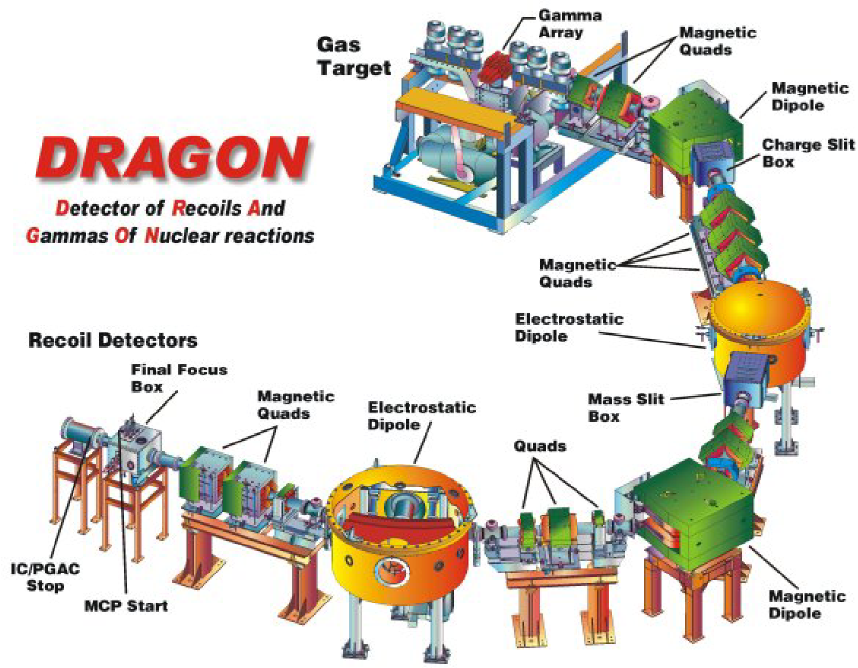

FIGURE 1.6: *A 3-D schematic representation of the DRAGON facility at TRIUMF.*

radioactive beam, produced at the ISAC facility, impinges on the DRAGON gas target, where a nuclear reaction may occur. Surrounding this gas target is an array of 30 BGO gamma detectors that detects prompt gammas from the reaction. From the gas target, both the recoils and beam particles continue together downstream and into the electromagnetic mass separator. Two stages of electromagnetic separation allows good separation and beam suppression. Once through the separator, recoils and any 'leaky beam' particles arrive at the end detectors for detection. These major system components are individually discussed in more detail in the following sections.

1.5.1 GAS TARGET AND BGO ARRAY

The DRAGON gas target is a differentially pumped, windowless target, which maintains either H_2 or He gas (for (p,γ) or (α,γ) reactions as appropriate) at between 4 and 8 Torr. Mounted within this gas target, at 30º and 57º to the beam direction, are two surface barrier silicon detectors, or elastics monitor, used for the detection of elastically scattered protons for use in determination of the total beam on target (as will be discussed at length later in this work). These detectors are highlighted in the schematic of the DRAGON gas target in figure 1.7. Surrounding the gas target is an array of 30 BGO (bismuth germanate) scintillator detectors, which detect prompt gammas emitted during nuclear reactions that may occur within the target [5]. A schematic of these detectors is shown in figure 1.8.

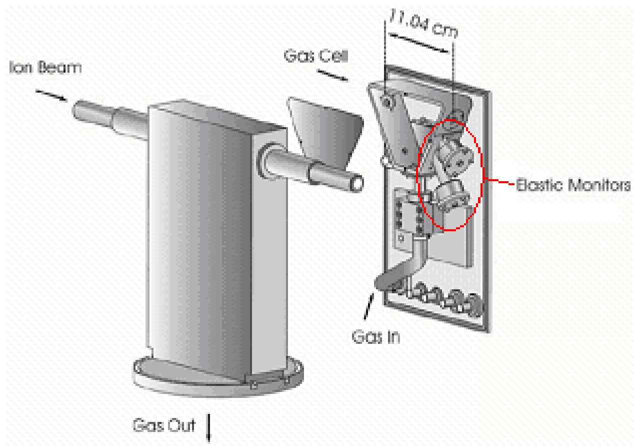

FIGURE 1.7: *A schematic of the DRAGON gas target, highlighting pair of surface barrier detectors.*

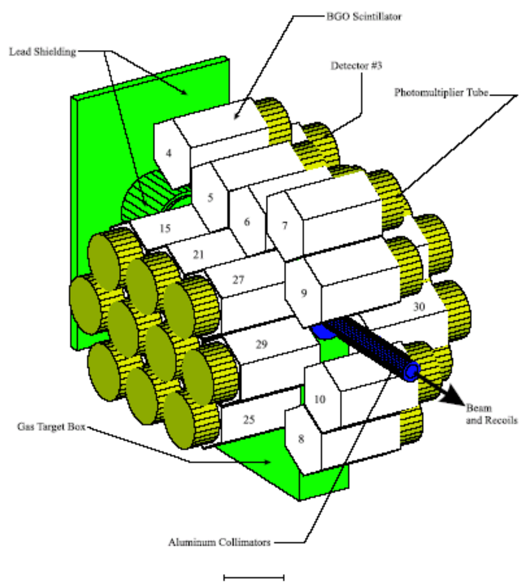

FIGURE 1.8: *A schematic of the BGO array surrounding the DRAGON gas target.*

1.5.2 ELECTROMAGNETIC SEPARATION

Owing to the fact that the reaction occurs in inverse kinematics, both the recoils and beam particles continue together downstream out of the target, with virtually the same momentum (conservation of momentum dictates that the recoils will have the same momentum as the incident beam particles with a very small spread due to the momentum kick from any prompt gamma rays) and into the electromagnetic mass separator. The DRAGON separator [4] has two separation stages, consisting of a magnetic dipole, focusing quadrupoles and an electrostatic dipole. The magnetic dipoles separate particles based on magnetic rigidity (mv/q), which, since all particles emerging from the gas target have virtually the same momentum, amounts to a separation based on charge state, isolating one charge state of recoils and beam particles. Magnetic quadrupoles then focus the beam, and are followed by electrostatic dipoles, which separate particles based on electric rigidity (mv^2/q), which amounts to a mass separation, since when particles reach this point, they have both the same charge and the same momentum. Two stages of separation allow improved separation and beam suppression, ideally lowering the background.

1.5.3 END DETECTORS

Once through the separator, recoils and any 'leaky beam' particles arrive at the end detectors. For the $^{26g}Al(p,\gamma)^{27}Si$ reaction, the end detector arrangement used involved a micro-channel plate (MCP) and a double-sided silicon strip detector (DSSSD). The MCP produces an electrical signal as a particle passes through, which was used to produce a timing signal with the DSSSD to give local time of flight information about the ions that arrived at the end detector. The DSSSD is a position sensitive, segmented semi-conductor diode detector, which offers a great deal of information during experiments, including the number and energy of particles detected, as well as positional information, and as was mentioned, local timing information when used in tandem with another detector. More information on these end detectors can be found in references [6-7].

1.5.4 CONTAMINATION DETECTORS

A final important component of the DRAGON system is a number of contamination detectors located at the mass slit box, located just downstream of the first electrostatic dipole. At these mass slits, a large portion of the beam particles that have made it through the separator to that point are deposited onto the mass slits, while the recoils from the reactions at the gas target continue through the system. A number of different contamination detectors are located monitoring the decay of the beam deposited onto these slits. For the $^{26g}Al(p,\gamma)^{27}Si$ reaction, the contamination monitors of interest were a pair of NaI detectors that monitored 511 keV annihilation photons, expected from the positron decay of the metastable isomer of ^{26}Al (a probable beam contaminant), and a high-purity germanium detector, which was set-up to monitor for the 1.809 MeV gamma ray characteristic of decaying ^{26}Na, another likely beam contaminant.

2 BEAM NORMALIZATION

As previously mentioned, a critical quantity in determining the thick target yield (and in turn resonance strength) is the number of incident beam particles on target. This requires not only a method for determining absolute beam intensity, but also knowledge of the relative beam intensity over the course of a run. This section explains how this task was achieved for the over 200 individual data runs taken.

2.1 PRINCIPLE OF NORMALIZATION

The determination of the number of ^{26g}Al particles on target over the course of any given run involved a number of steps. First, a measure of absolute beam intensity was determined, which was accomplished through the use of a Faraday cup located ~ 2 metres upstream of the gas target. However, since the Faraday cup stops beam during a measurement, the absolute beam intensity could only be measured at the beginning and end of a run. Given this, and the fact that beam intensity varies over the course of a two-hour run, the second step was to find a reliable monitor of relative beam intensity. The next section discusses the choice of such a monitor within the DRAGON system. Once this monitor was chosen, a relationship between the absolute beam intensity as measured at the Faraday cup, and the relative value measured by the monitor had to be determined to allow normalization of the beam intensity to the Faraday cup value. Finally, while this normalization provides the number of beam particles on target during a run, it does not provide the required information about the number of ^{26g}Al particles specifically. To determine this value, the levels of contaminant species, specifically ^{26}Na and ^{26m}Al, had to be determined, and subtracted.

2.2 BEAM MONITORS WITHIN DRAGON

Within DRAGON there are a number of potential beam monitors for use in beam normalization. For measurement of the absolute beam intensity, there are a total of 5 Faraday cups located at different positions along the length of the separator, including one ~ 2 metres upstream of the gas target, within the ISAC beam line, one just downstream of the gas target, one downstream of each of the charge slits and mass slits and one just before the end detectors. Concerning relative beam intensity determinations, as was previously mentioned, there are two elastics monitors located within the gas target, at 30° and 57° to the beam axis, which detect elastically scattered protons within the chamber. In addition, during the separation of particles through the separator, a significant portion of the beam particles (which are of lower mass than the recoils the separator is tuned for) are not bent as much within the electrostatic dipole and are deposited on the left mass slit, producing a current which can be monitored as an indicator of beam intensity. Other possible monitors of beam intensity include the signals from 'leaky beam' particles that make it through the separator and into the DSSSD end detector, as well as the signals from contamination monitors located in DRAGON as previously mentioned.

As has already been indicated, the Faraday cup located upstream of the gas target is the natural choice for absolute beam intensity determination, since this position allows measurement of the beam before it has been manipulated at all by the DRAGON separator. However, the more difficult task is the choice of a relative beam intensity monitor. The most natural beam monitor within the experimental system is the elastics monitor located within the gas target. The operational detector, located at 30° to the beam axis, views a path of hydrogen gas that the beam moves through, detecting Rutherford (Coulomb) elastically scattered protons, which are scattered by the larger beam particles as they move through the gas target. Rutherford scattering is a well-understood process, and the number of scattered protons depends directly on the number of incident beam particles, making this monitor an excellent choice. Figure 2.1 shows the clear beam intensity profile provided by this monitor over the course of a two-hour run. However, the elastics monitor is only useful when it is properly set. Unfortunately, for approximately 100 of the 250 runs taken during this experiment, the gains of this detector were incorrectly set, and it was not functional as a monitor of beam intensity. This means that it was necessary to establish a secondary beam intensity monitor, for which the best remaining choice was the current read on the left mass slit. While not ideal, due to some dependence on the tune of the system, and the fact that the mass slits are not electron-suppressed, the left mass slit does provide a good relative beam intensity profile, as is shown in figure 2.2, and was found to be an adequate beam monitor for the purposes of normalization.

2.3 Grouping of Experimental Runs

Before beam normalization could be performed, the 250 runs taken had to be grouped for analysis. Ideally, all of the runs would have been treated together, but upon inspection of some key values, it became clear that there were groups of runs that had to be treated independently from the others. Inspection of the FC1/FC4 ratio (FC1 refers to the Faraday cup located immediately downstream of the gas target, while FC4 refers to the Faraday cup located ~ 2 metres upstream of the target) showed two distinct groups of runs for which the ratio was much lower than expected, indicating a possible transmission problem through the target. The raw data for the FC1/FC4 ratio is provided in table A.1 in appendix A, and shown graphically in figure 2.3.

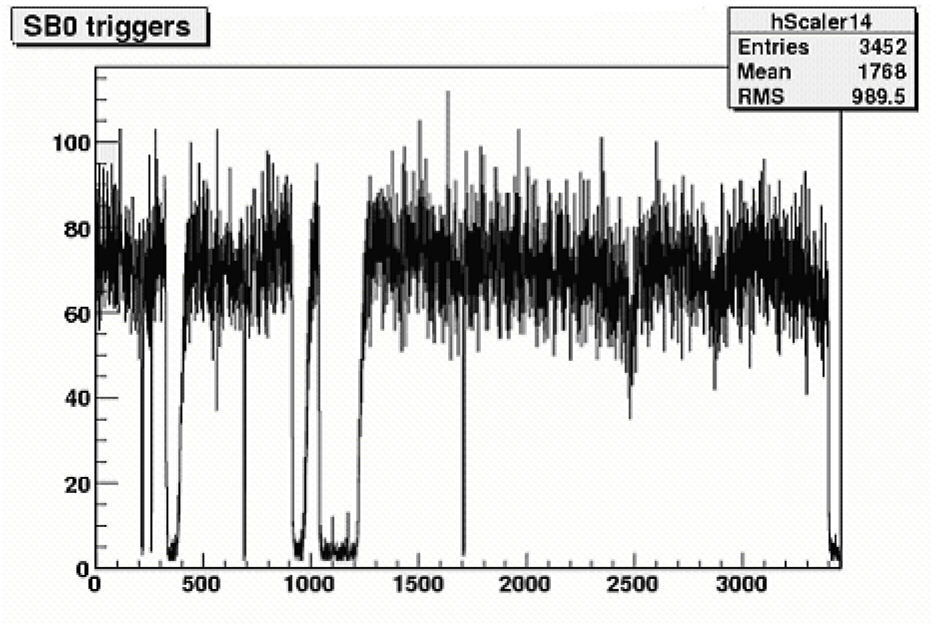

FIGURE 2.1: *A sample relative beam profile as generated by the triggers on the elastics monitor within the gas target.*

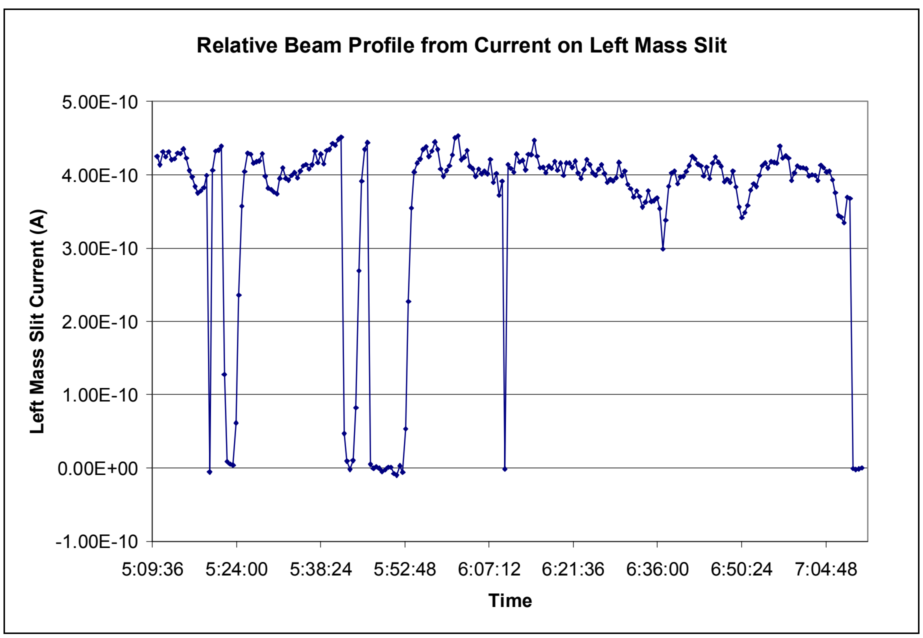

FIGURE 2.2: *A sample relative beam profile as generated by the current on the left mass slit.*

While no explanation for this problem has yet been found, for purposes of beam normalization these groups of runs were treated independently of the others.

Thus, beam normalization considered three distinct groups of runs, with one sub-group, as summarized in table 2.1 below.

Group of Runs	Run Numbers
1. "Good" runs	14843-14926, 14952-14983, 15030-15094
1. b. "Good" runs for use with elastics protons normalization method	14952-14983, 15030-15094
2. Poor transmission runs (before DSSSD change) – colour-coded as yellow runs	14927-14951
3. Poor transmission runs (after DSSSD change) – colour-coded as blue runs	14984-15029

TABLE 2.1: *Summary of groups of runs used in beam normalization analysis.*

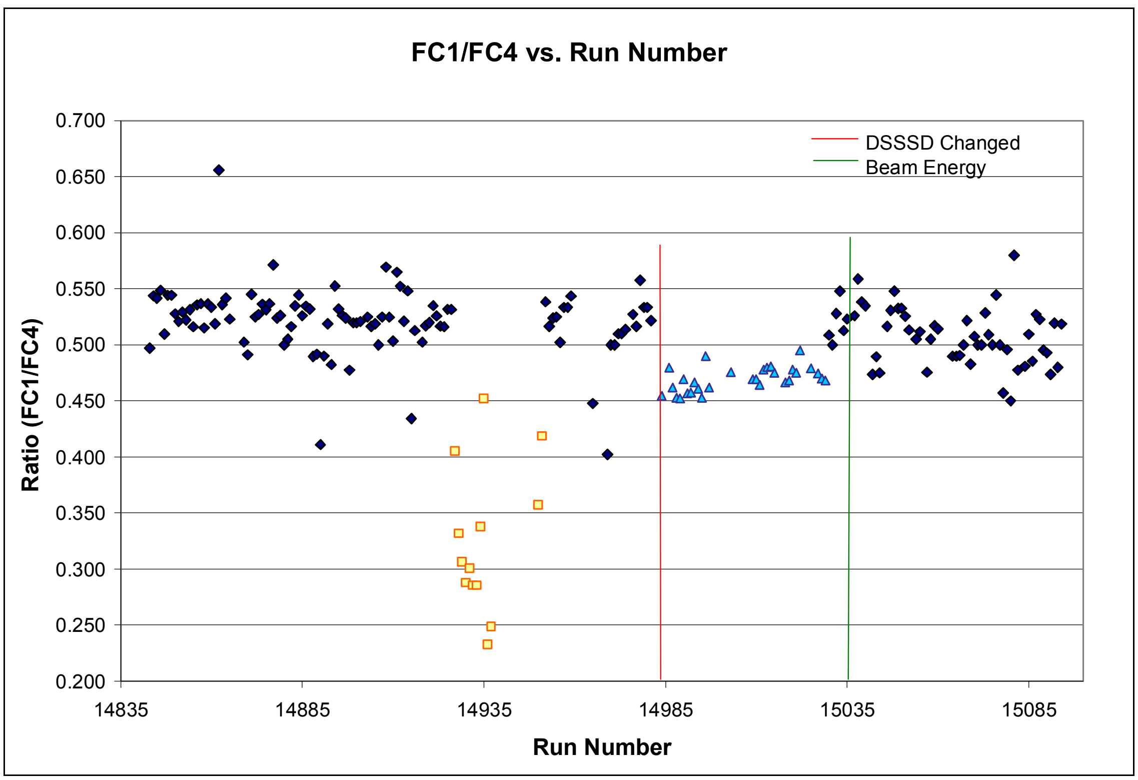

FIGURE 2.3: *FC1/FC4 ratio as a function of run number. Two groups of runs with low transmission are highlighted in yellow and blue.*

2.4 NORMALIZATION USING LEFT MASS SLIT

The current on the left mass slit is recorded by the MIDAS data acquisition system at 30 second intervals into a history file throughout an experiment, both during and between runs. When a run is started, the recording interval adjusts to ensure a reading that coincides with the beginning of the run. For purposes of beam normalization, these values were extracted from the history files (refer to appendix B for the command-line code used to extract the history information) and compiled into an EXCEL spreadsheet.

Beam normalization using the current on the left mass slit involved two distinct steps – establishment of a normalization factor relating the Faraday cup (FC4) absolute beam intensity reading to the current reading, and determination of the integrated charge on the left mass slit over the course of each run.

The logical normalization factor for this method of beam normalization was simply the ratio of FC4/Left Mass Slit Current as determined using the FC4 measurement made before the run was started, and the first left mass slit current reading in the history that was deemed to be a true representative value. In most cases, this was the first current value in the history corresponding to each run, though in a few situations a later current value was used (when it was apparent upon inspection of a graph of the left mass slit current value as a function of time that between the FC4 reading and the beginning of the run the beam intensity had dipped or spiked significantly). This ratio was calculated for every possible run (values are summarized in appendix A, table A.1), and the resulting values are plotted as a function of run number in figure 2.4. Average values were determined using standard formulae for each of the groups of runs as outlined in table 2.1. The resulting average normalization factors are presented in table 2.2.

GROUP OF RUNS	RUN NUMBERS	LEFT MASS SLIT NORMALIZATION FACTOR
1. "Good" runs	14843-14926, 14952-14983, 15030-15094	0.607 ± 0.005
2. Poor transmission runs (before DSSSD change) – colour-coded as yellow runs	14927-14951	0.94 ± 0.07
3. Poor transmission runs (after DSSSD change) – colour-coded as blue runs	14984-15029	0.667 ± 0.009

TABLE 2.2: *Summary of left mass slit normalization values for each group of runs.*

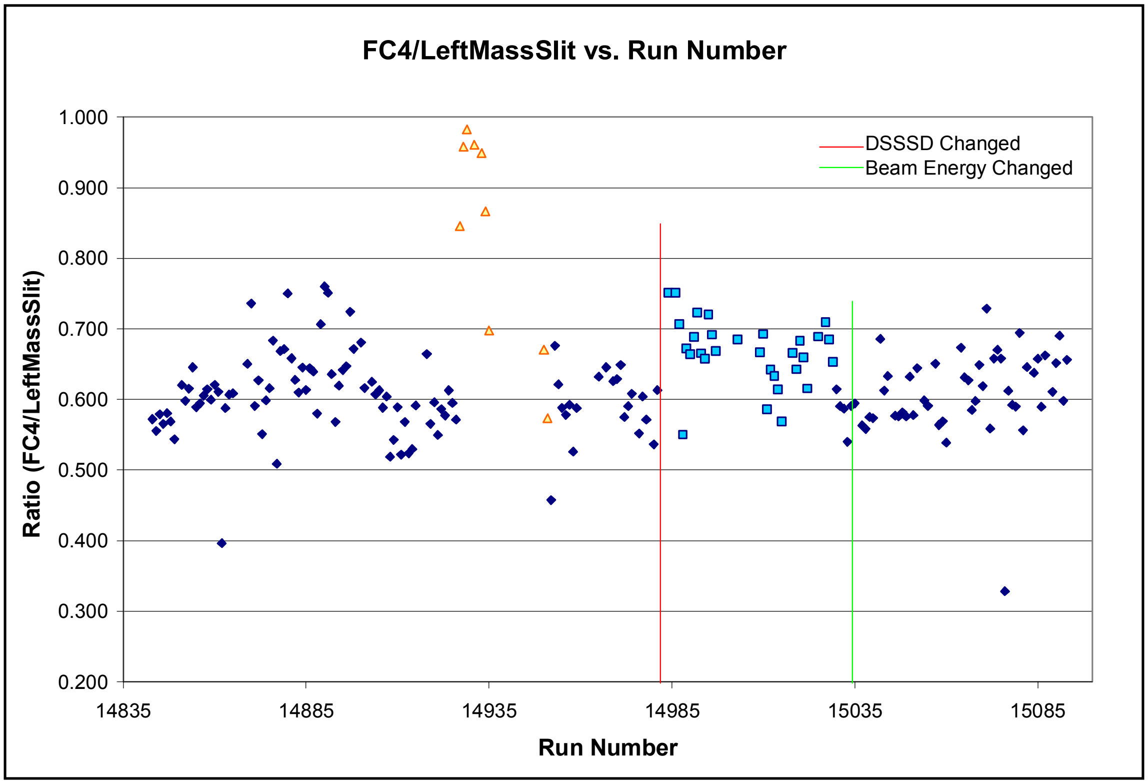

FIGURE 2.4: *FC4/Left Mass Slit ratio as a function of run number. The low transmission runs are highlighted in yellow and blue.*

Integration of the current on the left mass slit was carried out directly, using a relatively simplistic method. As was mentioned, current readings were taken at 30 second intervals, producing a run profile as was shown in figure 2.2. To integrate the area under such a curve, the average of each two consecutive current readings was taken, and multiplied by the 30 second interval it covered; the sum of each of the bars created was then taken to be the integrated value. This is graphically shown in figure 2.5. The error in the integrated value was estimated to be the same as the error in a single left mass slit current reading, or ~ 5% (determination of this value is included in appendix C).

Having established the integrated charge on the left mass slit, and a normalization factor relating the current to the FC4 reading, determination of the number of beam particles on target using this method required only application of the equation below:

$$\#\text{Beam Particles} = \frac{(\text{Integrated Charge on Mass Slit})(\text{Normalization Factor})}{(q \times e)} \tag{2.1}$$

where the q = is the charge state of the beam (6^+ in this case), and e is the fundamental unit of charge ($e = 1.6 \times 10^{-19}$ C).

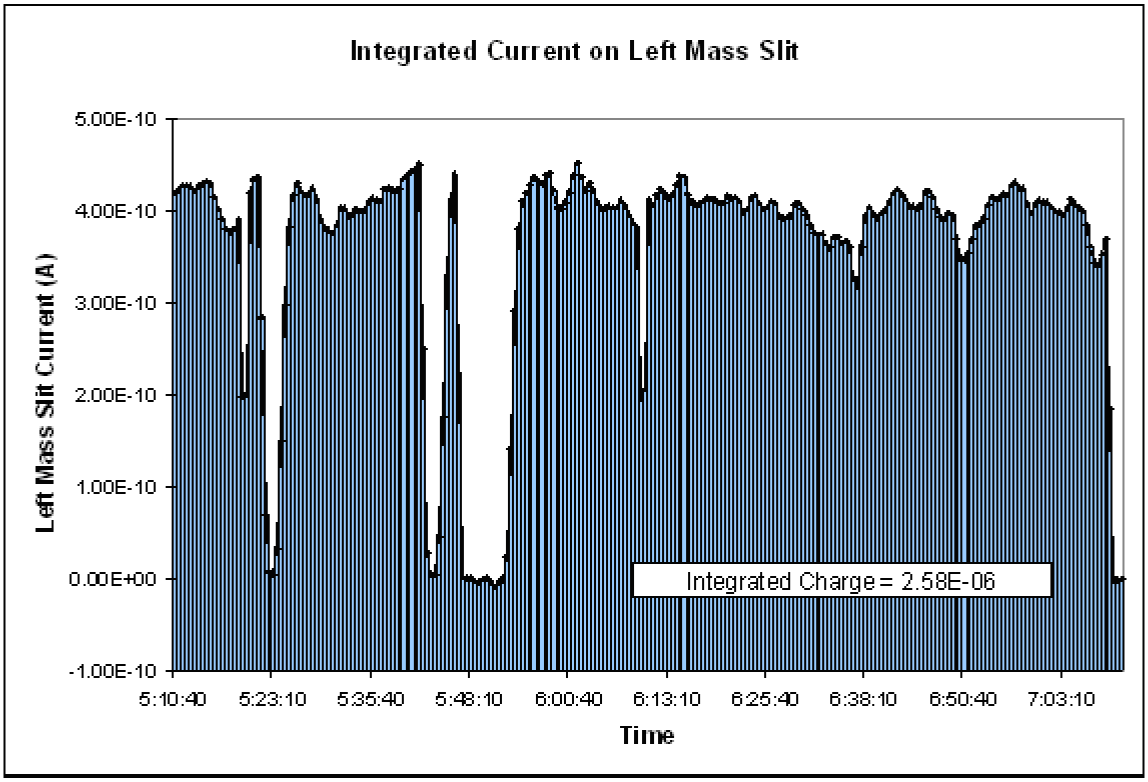

FIGURE 2.5: *A sample graphical representation of integration of left mass slit current.*

The run-by-run beam particles on target as determined using this method are summarized in table A.2 within appendix A. For a typical two-hour run, the number of beam particles on target was on the order of 10^{12}.

2.5 NORMALIZATION USING ELASTICALLY SCATTERED PROTON MONITOR

As was mentioned previously, the elastics monitor located within the gas target makes an excellent beam monitor and integrator through the detection of elastically scattered protons, the number of which depends on the number of incident beam particles to pass through the target over the course of a run. The equation for Rutherford scattering, presented below, is well known, and clearly shows this direct dependence of the number of scattered protons on the number of incident beam particles.

$$\#\,\text{Protons} = \#\,\text{Beam Particles} \times \#\,\text{Gas Particles/Area} \times \left(\frac{zZe^2}{4\pi\varepsilon_0}\right)^2 \times \left(\frac{1}{4E_{beam}^2}\right) \times \left(\frac{1}{\sin^4(\theta/2)}\right) \quad (2.2)$$

Similar to the use of the left mass slit, use of the elastics monitor as a beam normalization tool required determination of the total number of scattered protons over the course of the entire run (similar to the integrated left mass slit current), as well as establishment of a normalization factor relating the number of scattered protons to the actual number of beam particles on target.

Figure 2.6 shows a typical elastic monitor pulse height spectrum, focusing in on the area of interest in which the scattered proton peak is located. From this spectrum, the proton peak is very clear, and it is obvious that there is no significant background to worry about in determining the total number of elastically scattered protons. Thus, for the runs where use of the elastics monitor was possible, the total number of elastically scattered protons was easily determined through direct integration of the proton peak, over the range of 200-550. This integration was carried out more quickly using a macro for ROOT, the code[1] for which is included in appendix B.

Establishing a normalization factor relating the number of scattered protons to the actual number of beam particles on target was slightly more complicated than for the left mass slit method, but given the well-known dependence of Rutherford scattering on the gas pressure and beam energy, a more general normalization factor could be established that was independent of both of these quantities as variables. If the beam current was constant for a short period of time (300s) at the beginning of a run, and the number of scattered protons in the same time window could be determined, then an absolute normalization factor [8] was defined as follows:

$$R = \frac{I}{q \times e} \times \frac{\Delta t}{N_P \left(E_{beam}^2 / P\right)} \tag{2.3}$$

where I is the FC4 current reading taken before run, q is the charge of the beam particles (in this case, 6^+), e is the fundamental unit of charge ($e = 1.6 \times 10^{-19}$ C), Δt is the length of the short time interval (taken to be 300s), N_p is the number of elastically scattered protons within the short time interval, P is the pressure in the windowless gas target and E_{beam} is the beam energy in keV/u.

Values for this normalization factor were calculated only for runs in which the first 300s of the elastics monitor trigger rate spectrum showed a relatively constant beam intensity, as is the case in the spectrum shown in figure 2.7. When this criteria was met, the number of elastically scattered protons within the first 300s window was determined from the pulse height spectrum[2], and used in conjunction with the FC4 reading taken before the run to calculate a normalization factor. These calculated values are summarized in table A.3; the R-values, compensated for dead time (N_P is replaced by N_P/(%Live Time), where the % Live Time was determined from the ratio of presented tail triggers/observed tail triggers as found in the .odb run files), are plotted in figures 2.8 and 2.9 for the 'good' runs and the poor transmission (blue) runs respectively.

---

[1] Original macro was written by Benji Wales; modifications were made by this author.
[2] Data from the first 300s of the elastic monitor was evaluated and compiled by Lisa Fogarty.

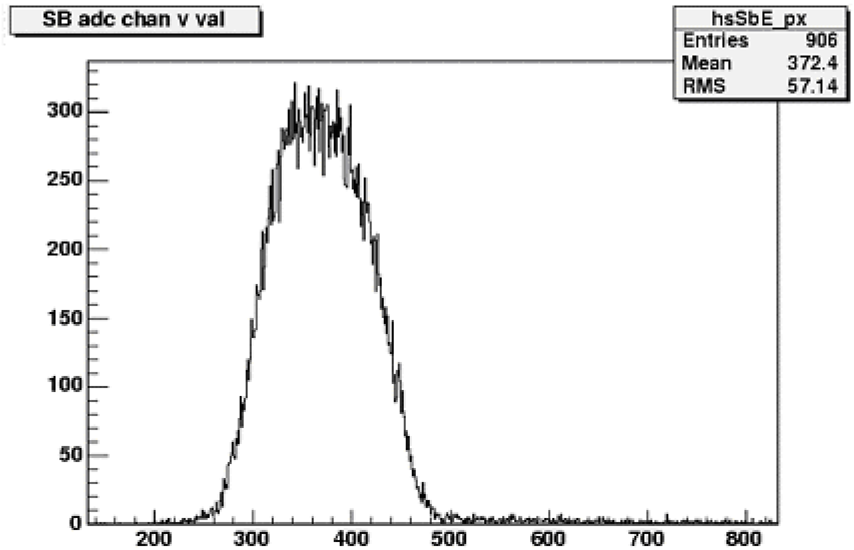

FIGURE 2.6: *A sample elastic monitor pulse height spectrum, focusing in on the elastically scattered proton peak.*

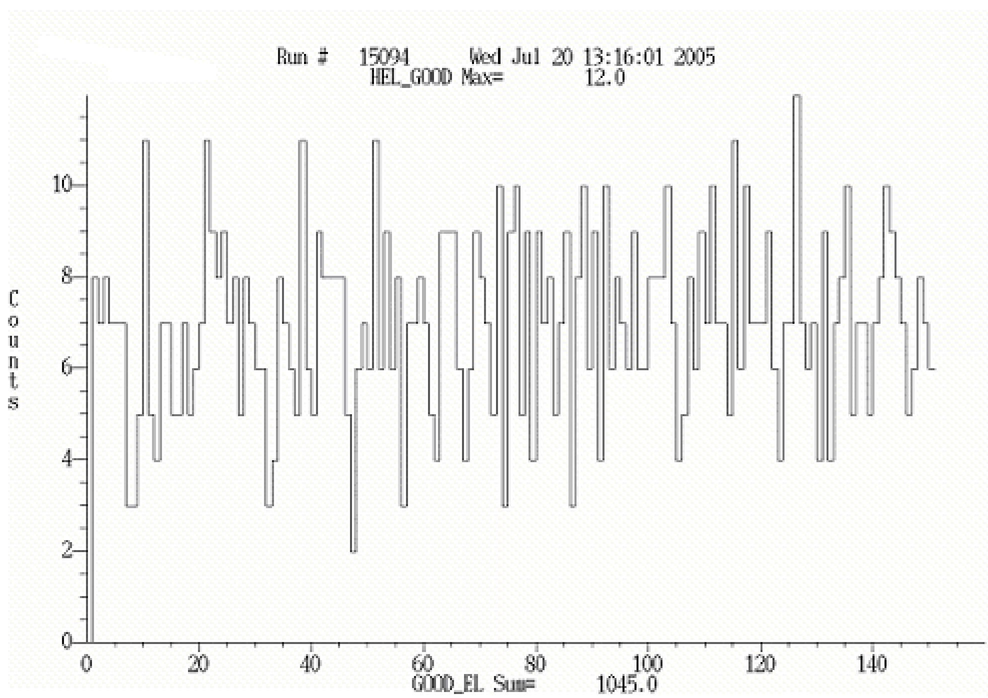

FIGURE 2.7: *A sample elastic monitor trigger spectrum, showing relatively constant beam intensity for the first 300s interval required for calculation of the normalization factor, R..*

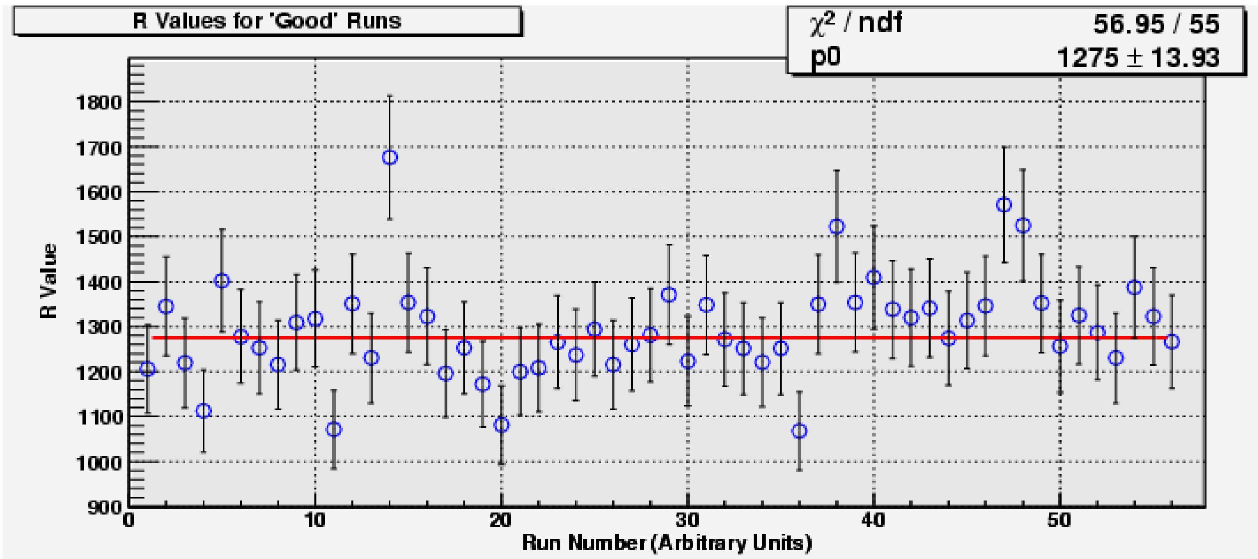

FIGURE 2.8: *Calculated normalization factors (R) for 'good' runs. Values have been compensated for the actual % live time as given by the presented/acquired tail triggers. Data is fit by a zero-order polynomial, producing a weighted average, confirmed by direct calculation in EXCEL.*

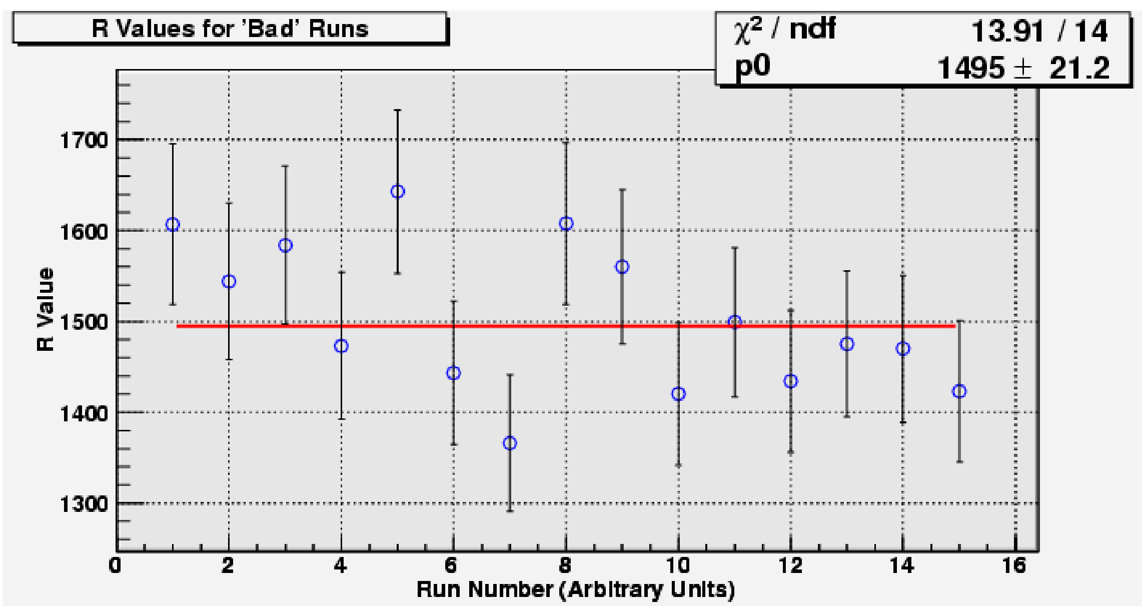

FIGURE 2.9: *Calculated normalization factors (R) for poor transmission (blue) runs. Values have been compensated for the actual % live time as given by the presented/acquired tail triggers. Data is fit by a zero-order polynomial, producing a weighted average, confirmed by direct calculation in EXCEL.*

By taking the weighted average of the calculated values, the absolute normalization factor is determined to be,

$$R_{\text{'good'}} = (1.276 \pm 0.015)\times 10^{3}\ {}^{26}\text{Al}\cdot\text{Torr}/\{\text{proton}\cdot(\text{keV/u})^{2}\}$$

for the ‘good’ runs and,

$$R_{\text{'bad'}} = (1.495 \pm 0.022) \times 10^{3}\ {}^{26}\text{Al}\cdot\text{Torr}/\{\text{proton}\cdot(\text{keV/u})^{2}\}$$

for the poor transmission (blue) runs. Having determined these normalization factors, calculation of the number of beam particles on target using this method required application of the following equation:

$$\#\ \text{Beam Particles} = \frac{R \times N_P \times \left(E_{beam}^{2} / P\right)}{\text{Run Duration}} \tag{2.4}$$

where N_p(total) is the total number of detected elastically scattered protons (compensated for live time), R is the absolute normalization factor as calculated previously, P is the average gas cell pressure, and E_{beam} is the beam energy in keV/u.

The run-by-run beam particles on target as determined using this method are summarized in table A.4 within appendix A. On average, for a two hour run, the number of beam particles on target was on the order of 10^{12}.

2.6 Beam Contamination

As was previously mentioned, calculation of the resonance strength requires the number of ^{26g}Al particles incident on the target over the course of the run, which is not necessarily, in fact likely not, the same as the number of beam particles. The radioactive ion beam delivered to DRAGON is not 100% pure ^{26g}Al – this beam is expected to contain isobaric contaminants such as observable nuclides, ^{26}Na and the metastable isomer of ^{26}Al, as well as unobservable ^{26}Mg. In order to determine the number of actual ^{26g}Al particles delivered on target, the number of contaminant particles must be determined as accurately as possible and subtracted from the total beam particles. This task required knowledge of the detection efficiencies of the contamination detectors used, as well as the charge state distributions of the contaminant species.

2.6.1 Calibration of Contamination Detectors

Of the three expected major beam contaminants, only two are easily observable. The metastable state of ^{26}Al, denoted by ^{26m}Al, decays directly to the ground state of ^{26}Mg through the emission of a positron. To detect this species, a ‘horn’ was placed above the mass slits on top of the mass slit box, with a pair of NaI detectors sitting next to it, one on either side. When the experiment is running, ^{26m}Al is deposited with other beam components onto the left mass slit, and then decays, emitting positrons, some of which make it into the horn and annihilate, emitting a pair of 511 keV gamma rays, which are detected, in coincidence, by the pair of NaI detectors. The other observable contaminant, ^{26}Na, undergoes beta decay with the emission of a characteristic 1.809 MeV gamma ray, to form ^{26}Mg, which is easily detectable using an HPGe detector pointed at the left mass slit, where this nuclide is also expected to be deposited during a run.

While these detectors were in place and had been previously used during an experiment, the detectors needed to be calibrated before and after the experiment, to determine detection efficiency, as well as to determine an energy calibration for the HPGe detector.

The NaI detectors were calibrated using a ^{22}Na calibration source[3] placed into the interior of the horn. The tab source was put into place by attaching it to the end of a flexible length of metal, which was introduced into the vented mass slit box through a removable port and manipulated into the horn. The coincidence trigger rate was determined with the source in the horn, as well as at the mass slits, which gave a background rate of accidental coincidences. To determine the horn detection efficiency this coincidence trigger rate was compared to the activity of the source, which was compensated for the time between the initial activity measurement date and the date of the efficiency determination according to the following formula,

$$A(t) = A_0 e^{-\lambda \times \Delta t} \tag{2.5}$$

where λ refers to the lifetime of the calibration source isotope, A_0 refers to the initial source activity, and Δt refers to the length of time between the efficiency measurement and the initial activity measurement. This same procedure was performed at the beginning and end of the experiment, giving horn detection efficiencies of (1.004 ± 0.020) % and (0.893 ± 0.020) % respectively. These horn detection efficiencies then had to be combined with the acceptance of the horn, calculated to be 6.35×10^{-4}, according to the schematic shown in figure 2.10. Combining the horn efficiencies and horn acceptance, and averaging the two absolute efficiencies, the detection efficiency of the pair of NaI detectors for ^{26m}Al was taken to be $(6.00 \pm 0.57)\times10^{-6}$.

The HPGe detector required a slightly more intensive calibration, since it required both energy and efficiency calibration. This detector was calibrated using 3 calibration sources[4] emitting gammas over the energy range of 511 keV to 1836 keV. At both the beginning and end of the experiment, in separate runs, a ^{22}Na, a ^{60}Co and an ^{88}Y source were secured in position on the left mass slit where beam particles are expected to be deposited, and a spectrum was collected

[3] Na-22 solid, TRIUMF R-00600.8, 3.65e+05Bq, 01/Jul/03

[4] Na-22 solid, TRIUMF R-00600.8, 3.65e+05Bq, 01/Jul/03, Co-60 solid, TRIUMF R-00600.5, 3.91e+05 Bq, 01/Jul/03, Y-88 solid, TRIUMF R-00600.9, 3.63e+05Bq, 01/Jul/03

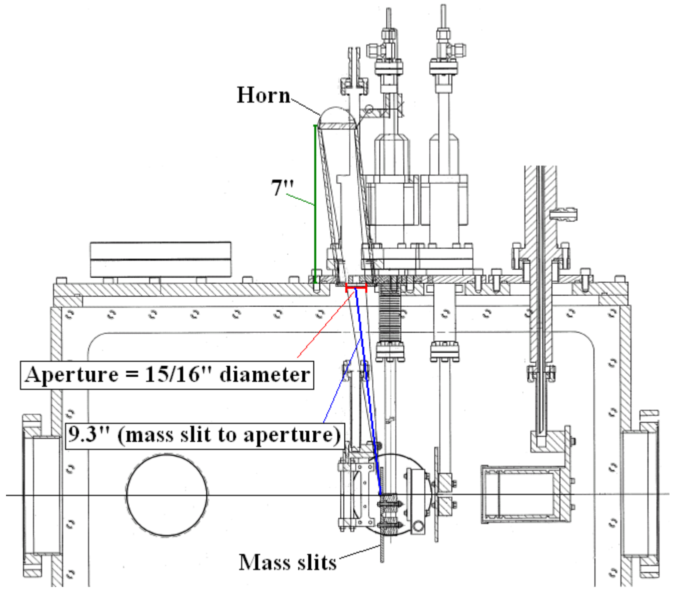

FIGURE 2.10: *Schematic of the mass slit box and horn assembly used in calculation of the horn positron acceptance.*

using the germanium detector. The length of the runs was dependent on the strength of the source, and ranged from approximately one hour to 16 hours (overnight). A background run was also taken to determine the room background. Energy calibration was then completed by manually fitting Gaussians to the peaks in each spectrum, and using a macro to plot the channel numbers of the peaks versus the gamma energies, and fitting a first-order polynomial, to produce a calibration curve. The code for the energy calibration macro is included in appendix B. The calibration curve for the post-experiment energy calibration is shown in figure 2.11.

Efficiency calibration of the HPGe detector was carried out by determining the integral of the gamma peaks, and converting this integral into a rate using the duration of the each run. A background rate as determined from the background run was then subtracted, and the net counting rates for each gamma energy was compared to the decay rate of the calibration source, again adjusted for the time passed using equation 2.5, as well as for the probability of gamma emission. This gave efficiency for the detection of each gamma, the natural logarithm of which was then plotted versus the natural logarithm of the gamma energy and fit with a first-order polynomial to produce an efficiency calibration curve (code for this calibration is included in appendix B). Figure 2.12 shows the pre-experiment efficiency calibration curve. However, during this experiment the efficiency of interest was that for the detection of the 1.809 MeV gamma ray emitted in the decay of ^{26}Na, which are close in energy to the highest energy gamma emitted in the decay of ^{88}Y, 1.836 MeV. Averaging the pre- and post-experiment efficiencies for the detection of this gamma ray gave an absolute detection efficiency for ^{26}Na of $(1.23 \pm 0.10)\times10^{-5}$.

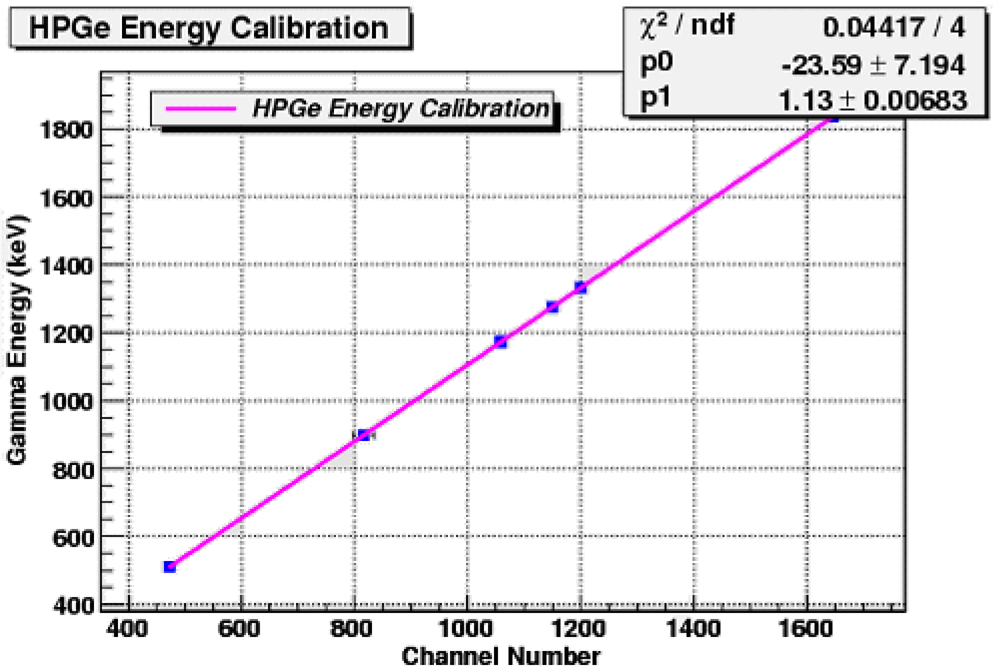

FIGURE 2.11: *HPGe energy calibration curve from post-experiment calibration.*

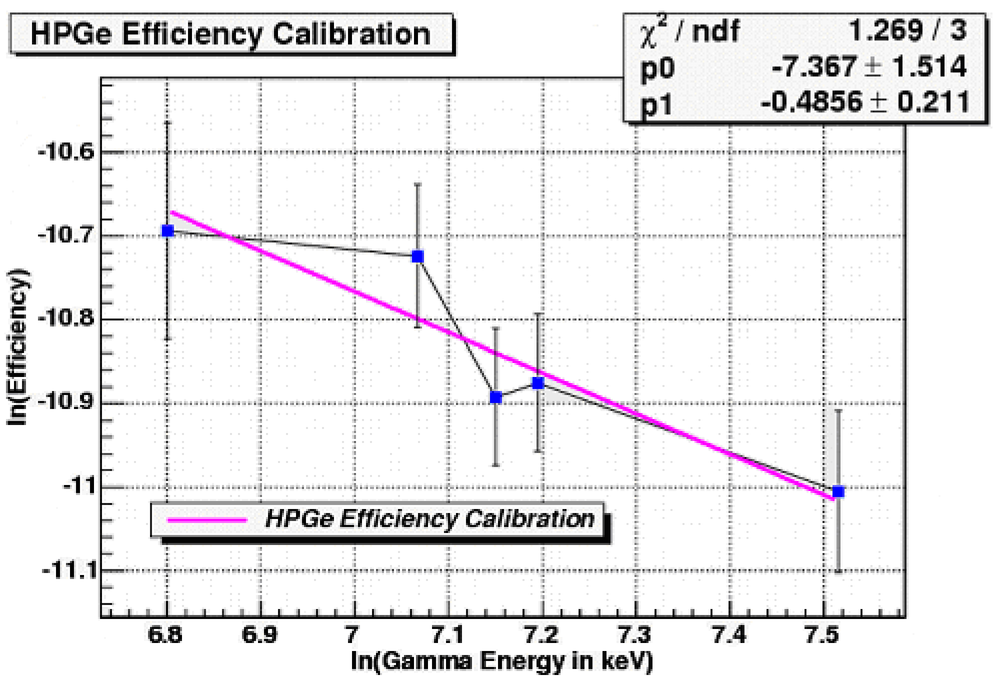

FIGURE 2.12: *HPGe efficiency calibration curve from pre-experiment calibration.*

2.6.2 CHARGE STATE DISTRIBUTION OF CONTAMINANTS

In addition to a detection efficiency, which is used to determine the number of contaminant particles that are deposited at the mass slits, it is important to know what portion of the particles that represents, or in other words, the percentage of the contaminant particles expected to have the correct charge state to make it past the charge slits and to the mass slit box after emerging from the gas target. This requires knowledge of the charge state distributions for ^{26}Na and ^{26m}Al in the 4^+ charge state, the recoil charge state for which DRAGON was tuned.

While beam particles start out in a 6^+ charge state, after traversing the gas target and having charge-exchanging collisions with the gas molecules, beam particles emerge with a distribution of charge states. Studies of charge state distributions for various ions, beam energies and gas pressures were investigated in the work of Liu [9]. In this work, the equilibrium charge state distribution for sodium was directly measured, and for a beam energy of 200 keV/u, very similar to the beam energy used in the experiment, the probability for the 4^+ equilibrium charge state (equilibrium is assumed to be reached with the 6 Torr gas target pressure used) was determined to be 40.78 ± 1.20 %. While the equilibrium charge state distribution for aluminum was not directly measured, this work also determined that charge state distributions were well described by a Gaussian parameterized with a mean charge state and an approximate width. An empirical equation for the mean charge state (charge state of the highest probability) was determined as given below,

$$\bar{q} = Z_P \times \left[1 - \exp\left(-\frac{A}{Z_P^{\gamma}} \sqrt{\frac{E}{E'}} + B \right) \right] \tag{2.6}$$

where Z_P is the beam particle atomic number, E is the beam energy, in MeV/u, E' = 0.067635 MeV/u, and A, B, and γ are free parameters that were fit to the experimental data and found to take the following values: A = 1.4211, B = 0.4495 and γ = 0.44515. For aluminum, the highest probability charge state was calculated to be 3.66^+. The work also presented an empirical formula for determination of the width, but in practice the width is better estimated through interpolation of experimental data. Given that no data was available for Al, Mg data was used to estimate a distribution width of 0.711. Using this width with the calculated average charge state to construct a Gaussian approximation for the charge state distribution, and estimating 5% error in the determination, the probability for the 4^+ equilibrium charge state for ^{26m}Al was determined to be 50.05 ± 2.50 %.

2.6.3 ^{26}Na AND ^{26m}Al BEAM CONTAMINATION

Having determined the efficiency of the contamination detectors, as well as the probability of the contaminant particles being in the 4^+ charge state, the amount of ^{26}Na and ^{26m}Al contaminant could be determined.

^{26m}Al was quantified by determining the number of NaI coincidence triggers over the course of each run, and subtracting the number of random coincidence triggers (scaled for the length of the run) as determined from a background run. This net number of coincidence triggers was then divided by the absolute detection efficiency previously determined, as well as the charge state fraction, according to the following formula, to determine the number of ^{26m}Al particles contained within the beam.

$$\#^{26m}\text{ Al Particles} = \frac{\text{Coincidence Triggers}}{\text{Absolute Efficiency} \times \text{CSF}} \tag{2.7}$$

On average, for the bulk of the runs, which did not have the benefits of laser ionization in the beam production, the ^{26m}Al contaminant level was 0.01%. The contamination levels of ^{26m}Al on a run-by-run basis are shown graphically in figure 2.13.

^{26}Na was similarly quantified by determining the integral of the 1.809 MeV gamma peak in the HPGe spectrum for each run, and subtracting the integral from the background run (scaled for the length of each run). This integral was then divided by the detection efficiency previously determined and the charge state fraction to determine the number of ^{26}Na particles, according to the following formula.

$$\#^{26}\text{ Na Particles} = \frac{\text{Gamma Peak Integral}}{\text{Absolute Efficiency} \times \text{CSF}} \tag{2.8}$$

For the majority of runs, which did not have laser ionization, the ^{26}Na contaminant level was 0.6%. Figure 2.14 shows a run-by-run graph of the ^{26}Na contamination level.

2.7 FINAL RESULTS AND CONCLUSIONS

Having determined the total number of beam particles on target for each run, as well as the number of ^{26}Na and ^{26m}Al contaminant particles, calculation of the actual number of ^{26g}Al beam particles on target was straight-forward. Subtraction of the number of contaminant particles from the total number of beam particles as determined using the elastics monitor was done where possible to determine the total number of ^{26g}Al particles on target; where a normalized beam from the elastics monitor was not available, the value from the left mass slit calculation was used. This

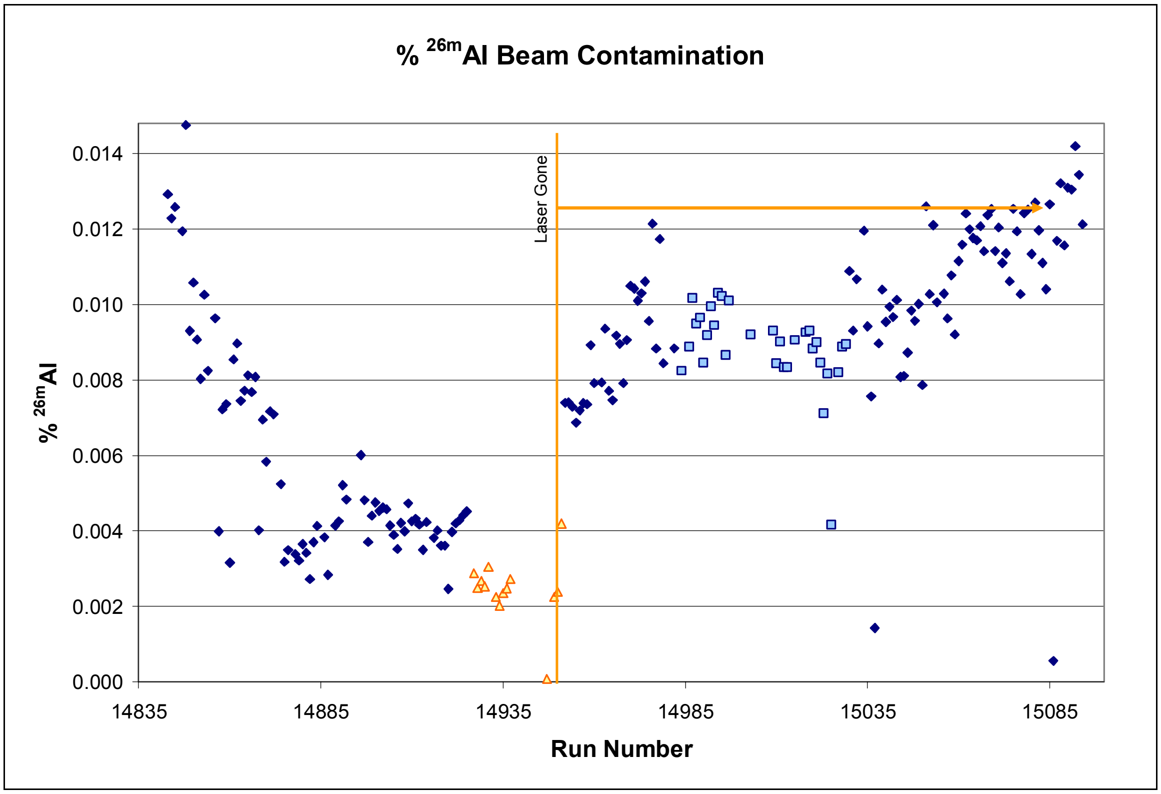

FIGURE 2.13: *Run-by-run % ^{26m}Al contamination in beam.*

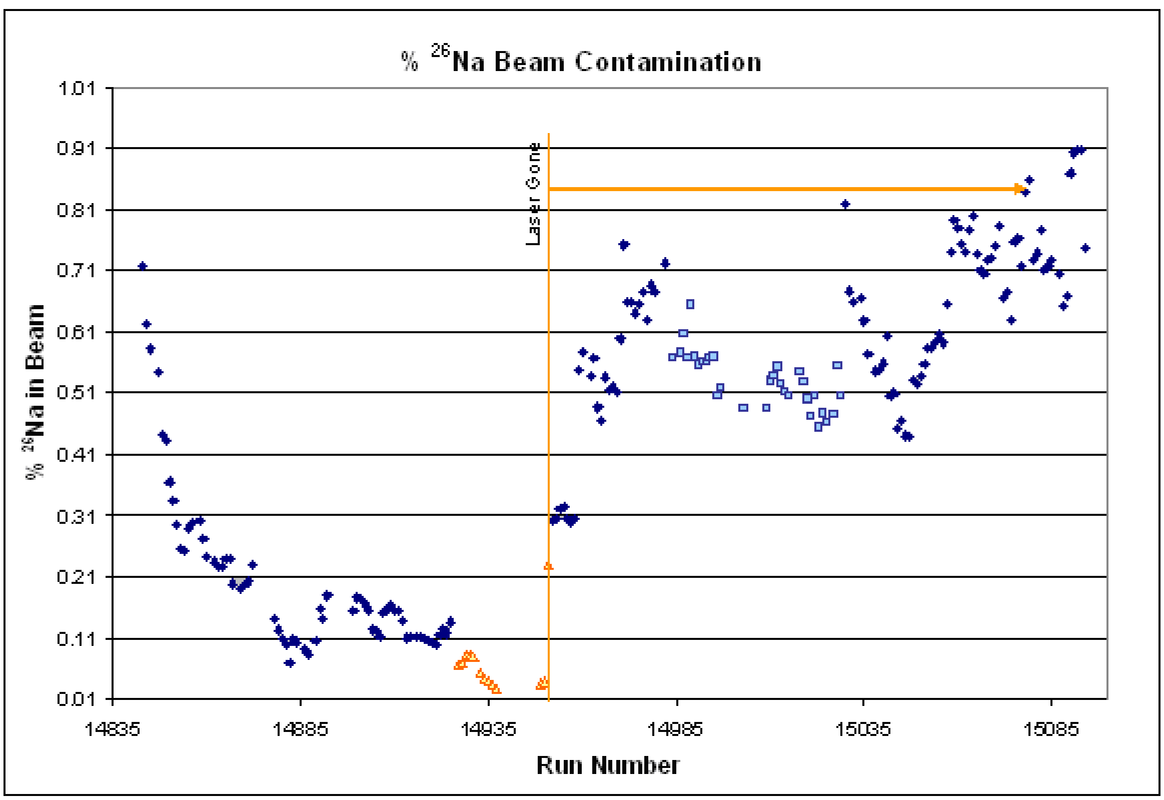

FIGURE 2.14: *Run-by-run % ^{26}Na contamination in beam.*

alternate method was validated by the fact that for the approximately 140 runs where both methods were used the agreement between the two normalized beam values was within 8%.

The final run-by-run normalized ^{26g}Al beam particles on target is provided in table A.5 in appendix A[5].

While the left mass slit method did allow beam normalization, the elastics monitor method is viewed as more reliable; given this, an important step in preparation for an experiment should include checking that the elastics monitor is properly set-up, so that elastics data is available for all runs. In addition, to avoid the requirement of treating groups of runs differently due to unexplained problems (such as the apparent poor transmission groups within this experiment), certain ratios should be more carefully monitored while running, including the FC1/FC4 ratio.

[5] Alternatively, all data found in appendix A, as well as additional run-by-run information has been compiled in an EXCEL spreadsheet available on ibm00 in home/hcrawfor/Public/26Alpg/Master Run Data.xls.

3 BGO Gamma Array Efficiency

The DRAGON system, as the acronym suggests, is a detector of both the recoils and gamma rays emitted in nuclear radiative capture reactions. While recoils are detected at the end detectors, after being separated from beam particles in the separator, gamma rays are detected at the BGO gamma array surrounding the gas target, as previously described. Thus, as is shown by equation 1.5 for the experimental thick target yield, the BGO array detection efficiency for the gamma rays emitted in a given reaction is a critical quantity. To determine the detection efficiency, a GEANT (**GE**ometry **AN**d **T**racking) simulation of the DRAGON gas target and BGO array was used to simulate reactions, and the detection of the resulting gamma rays. A number of simulations were run for different possible simple gamma angular distributions, in order to determine a general averaged BGO efficiency.

3.1 Gamma Emission in the $^{26}Al(p,\gamma)^{27}Si$ Reaction

When a ^{26}Al particle captures a proton, it forms an excited state of ^{27}Si, as was shown in figure 1.3. This excited state then decays, through gamma emission, to the ground state. The gamma emission is nearly simultaneous with the proton capture, and thus occurs when the newly formed ^{27}Si nucleus is still within the gas target, surrounded by the BGO array. This decay proceeds through well-defined energy states in the ^{27}Si nucleus, resulting in the emission of gamma rays of well-defined energies. Figure 3.1 shows an energy level diagram for ^{27}Si, where the Q-value (the amount of energy released during the ^{26}Al + p fusion) for the reaction is indicated, along with the resonance state that was populated in the experiment, the 188 keV resonance level (which corresponds to the 7.653 MeV excited state in ^{27}Si). Also shown in figure 3.1 are the possible gamma decays important for decay from the 7.653 MeV excited state populated in this experiment. This excited state of ^{27}Si undergoes cascade gamma decay, meaning that to reach the ground state, rather than decaying directly to this state, the nucleus moves through a number of intermediate excitation levels first, thus releasing a series, or cascade, of gamma rays along the way. However there is not just one possible decay path and while it is impossible to know which decay path a given excited ^{27}Si nuclide will take, probabilities known as branching ratios can be assigned to each possibility. These branching ratios are also indicated in figure 3.1 for the relevant gamma decays.

Thus, if one considers all possible decays paths for the 7.653 MeV excited state in ^{27}Si, it is evident that there are five different gamma cascades expected from this excited state. These possible cascades, and their respective probabilities are summarized in table 3.1.

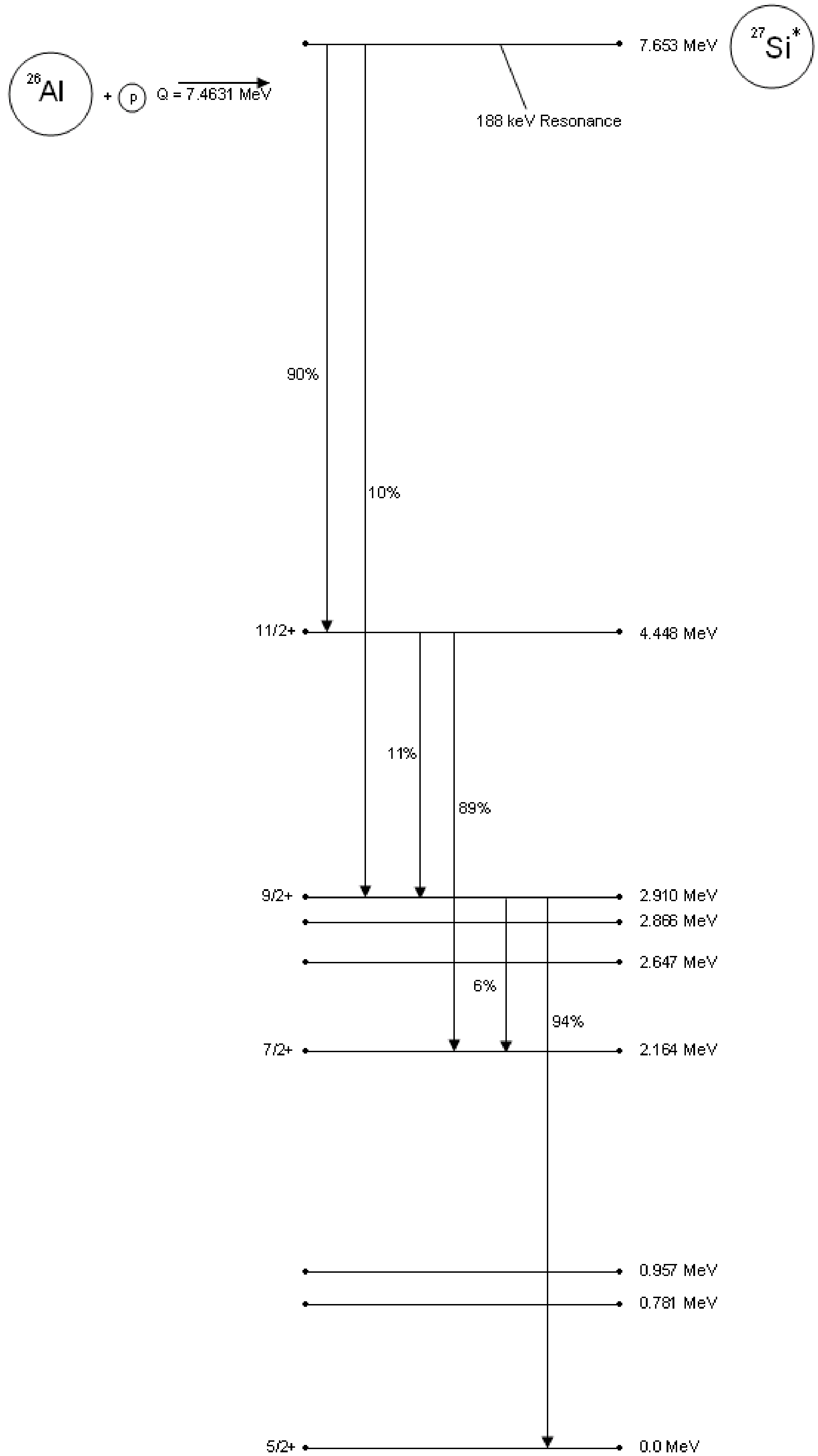

FIGURE 3.1: *Level scheme for ^{27}Si, indicating the 188 KeV resonance, the Q-value for the proton capture reaction and the gamma decays and branching ratios relevant to decay from the 7.653 MeV excited state.*

Gamma Cascade	Probability of Cascade	Primary Gamma (MeV)	Secondary Gamma (MeV)	Third Gamma (MeV)	Fourth Gamma (MeV)
Cascade A (through 11/2+ and 7/2+ to ground)	80.10 %	3.205	2.284	2.164	--
Cascade B (through 11/2+, 9/2+ and 7/2+ to ground)	0.59 %	3.205	1.538	0.746	2.164
Cascade C (through 11/2+ and 9/2+ to ground)	9.31 %	3.205	1.538	2.910	--
Cascade D (through 9/2+ to ground)	9.40 %	4.743	2.910	--	--
Cascade E (through 9/2+ and 7/2+ to ground)	0.60 %	4.743	0.746	2.164	--

TABLE 3.1: *The five possible gamma cascades from the 7.653 MeV level populated in the $^{26}Al(p,\gamma)^{27}Si$ 188 keV resonance reaction.*

However, in considering the efficiency of the BGO gamma array, the quantity of interest is the weighted, averaged efficiency for all possible gamma decays. This is the quantity that is determined using the GEANT simulations of the BGO array as described in the next section.

3.2 GEANT SIMULATION AND GAMMA SPECTRA ANALYSIS

The GEANT simulation of the DRAGON BGO array, which is described in detail in reference [5], can be used to simulate the detection of the cascade gamma rays emitted in reactions occurring within the gas target. As input, from a number of input files, such as those included in appendix B, the simulation takes the relevant data for the gamma cascades (including the branching ratios for decay from each excited state, and the lifetime of each excited state) as well as the number of reactions desired and the angular distribution of the gamma radiation. As output, the simulation produces (among other things) a histogram of the energies of detected gamma rays in the BGO array. In fact, the simulation produces a number of histograms, including a histogram of the highest energy (first) gamma ray detected in a cascade only, as well as a histogram for the second highest energy gamma and for the sum of the first two gamma rays.

In determining the BGO efficiency, the histogram of interest is that of the highest energy gamma ray detected, due to the thresholds set for the BGO array. The BGO array has a trigger threshold which during the $^{26}Al(p,\gamma)^{27}Si$ experiment was set, over different sections of runs, to 2 MeV and 1.75 MeV. This threshold is the minimum energy required of the highest energy gamma to allow all other radiation to be registered. In other words, if the highest energy gamma ray of a group of incoming radiation is higher than this threshold, all gammas in the group will be registered; if not, no gammas will be detected. There is also a secondary threshold, which is included in the GEANT simulation, that all incoming gamma radiation must exceed, which serves to reduce low energy background. Thus, the cascade radiation emitted in a reaction will be detected only if the highest energy gamma emitted is above the threshold. To determine the BGO efficiency, the number of gammas above threshold in the first gamma spectrum is compared to the total number of reactions that occurred.

The simulation was run for three different simple angular distributions, which are summarized in table 3.2 below. 5000 events were simulated for each angular distribution, producing first gamma spectra like that shown in figure 3.2. However, these simulated spectra do not include detector resolution. Thus, before BGO efficiency could be considered, detector resolution had to be incorporated [10]. This was done by convolving the raw GEANT output with gaussians, whose width varies according to the following well-known energy dependent formula:

$$\mathrm{FWHM} = k\sqrt{\mathrm{E}} \tag{3.1}$$

where k = 0.173 and E is the gamma energy in MeV. The C++ code for this convolution is included in appendix B. Figure 3.3 shows a sample convolved first gamma spectrum.

Isotropic (L=0, M=0)	1
Dipole (L=1, M=0)	$(3/8\pi)\sin^2\theta$
Quadrupole (L=2, M=0)	$(15/8\pi)\sin^2\theta\cos^2\theta$

TABLE 3.2: *The three simple angular distributions considered in the GEANT BGO simulations.*

After convolving the GEANT spectra to simulate detector resolution, determination of the BGO efficiency depends on establishing the detector threshold. While the thresholds are theoretically 'hard' thresholds, with gamma rays either satisfying the criteria or not, in actual fact, they are somewhat 'soft', approximating a half-gaussian, centered near the set threshold value. Thus, in considering BGO efficiency, a number of approaches were considered. Using background spectra for the 2 MeV threshold, the shape of the threshold was approximated by a gaussian, as is shown in figure 3.4, and applied to the GEANT simulated spectra. For the 1.75 MeV threshold level, a gaussian of the same width as the 2 MeV threshold, but centered at a lower energy was used to approximate the actual shape. As an alternative to approximating the actual threshold shape, a hard cut at the upper energy of the threshold was also considered for both energies, which would have to be implemented in data analysis as well, for these efficiencies to be of use. Figures 3.5 through 3.8 illustrate the various thresholds considered in determining the BGO efficiency.

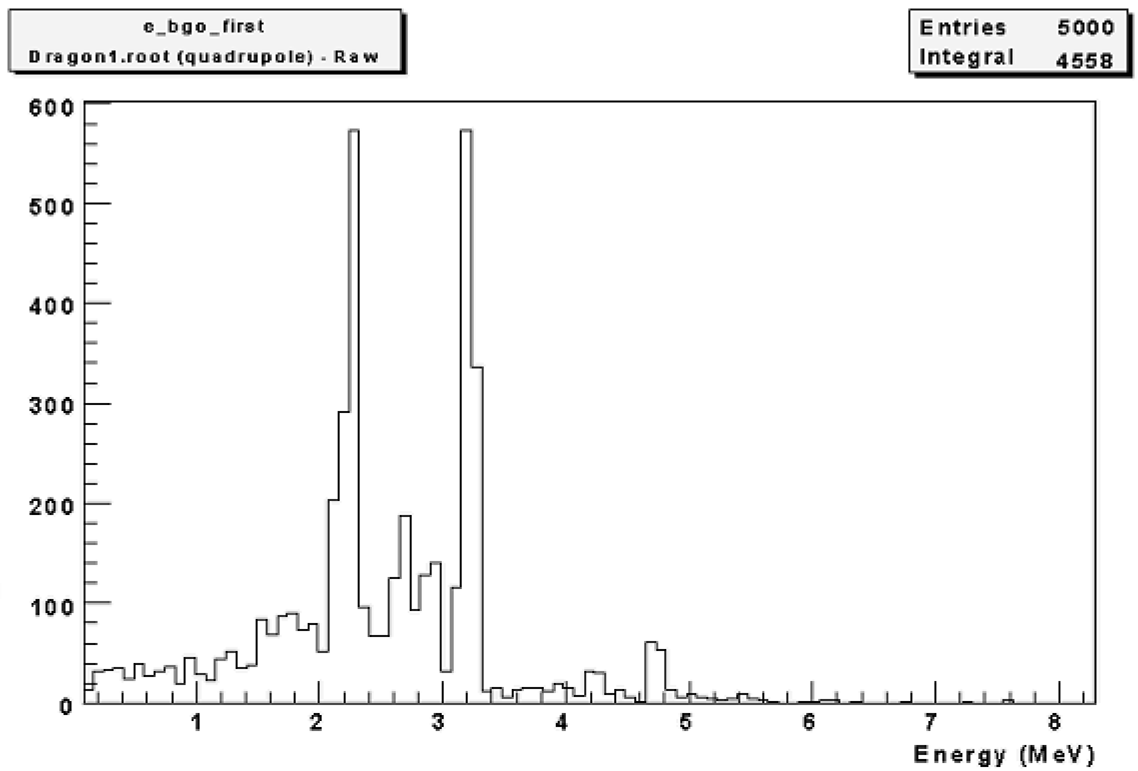

FIGURE 3.2: *Sample GEANT first gamma histogram without any manipulation (quadrupole angular distribution).*

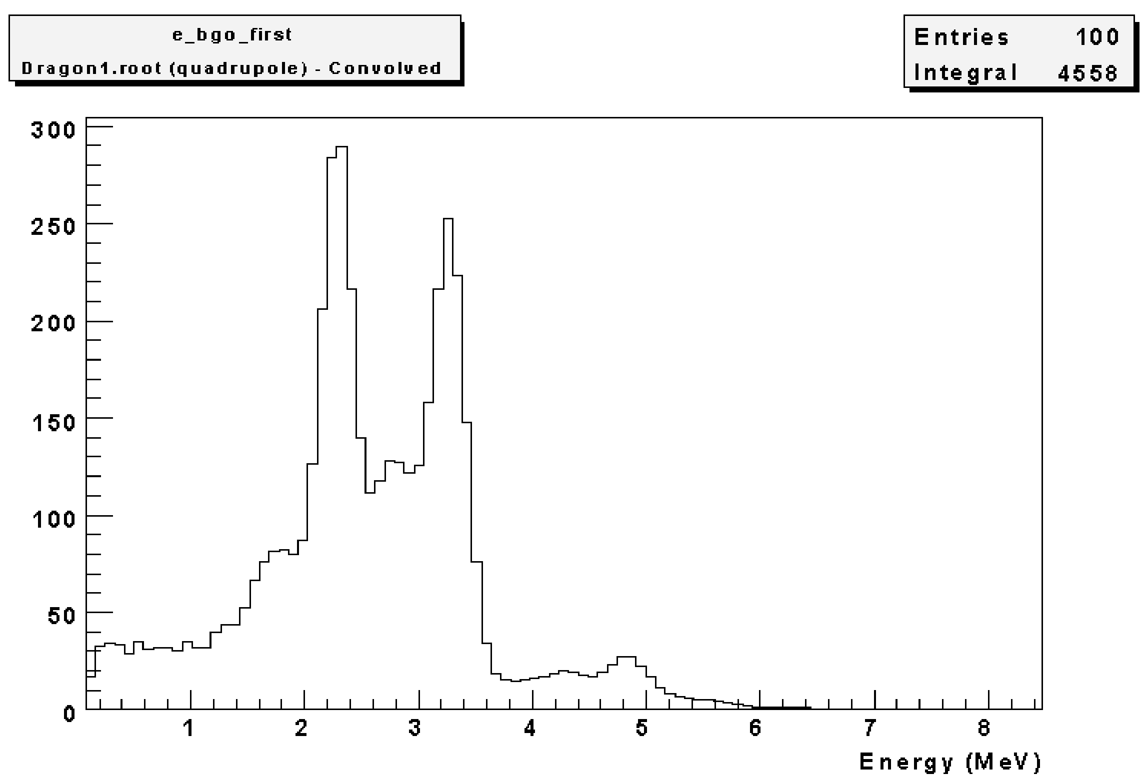

FIGURE 3.3: *Sample first gamma histogram after convolution with gaussians to approximate detector resolution (quadrupole angular distribution).*

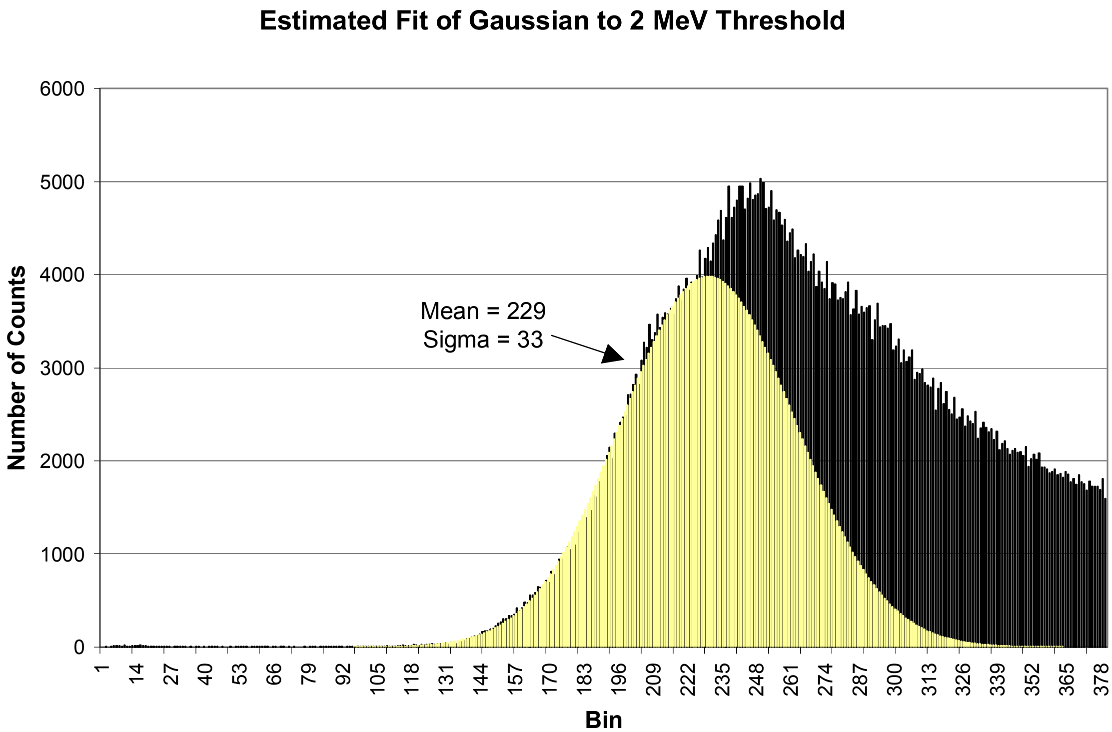

FIGURE 3.4: *Background spectrum with 2 MeV threshold illustrating gaussian approximation for shape of the threshold.*

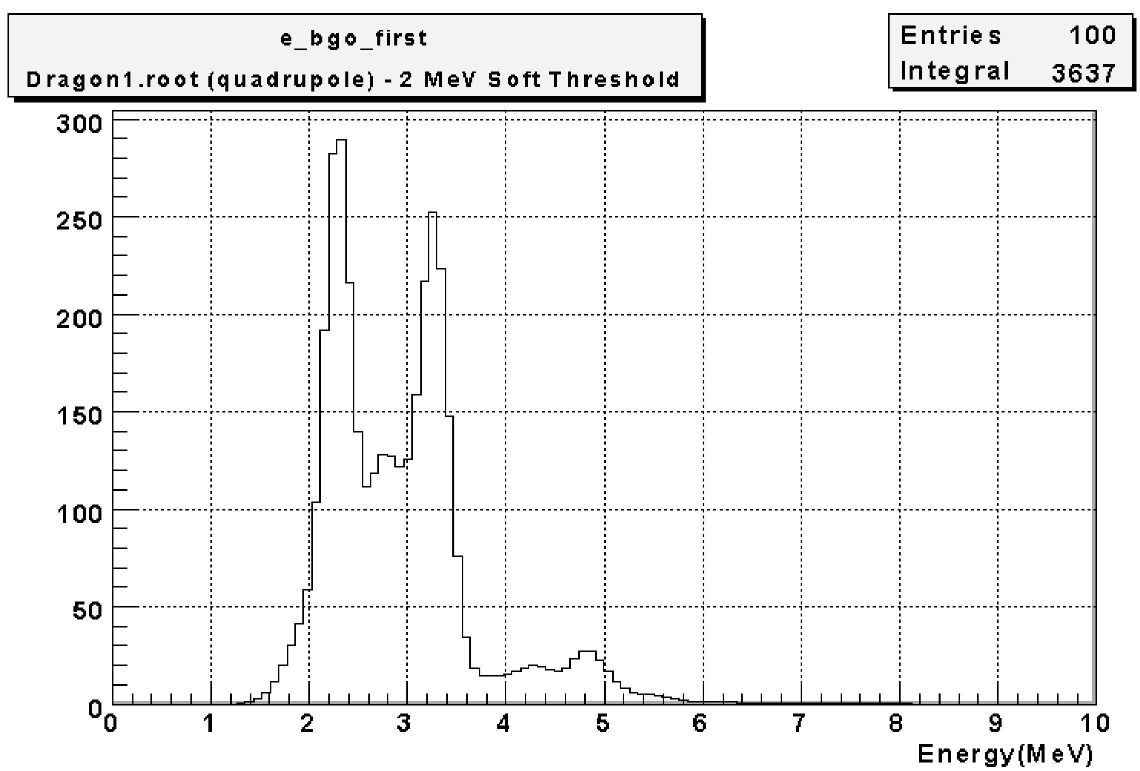

FIGURE 3.5: *Sample first gamma histogram after convolution with gaussian and application of 2 MeV shaped threshold (quadrupole angular distribution).*

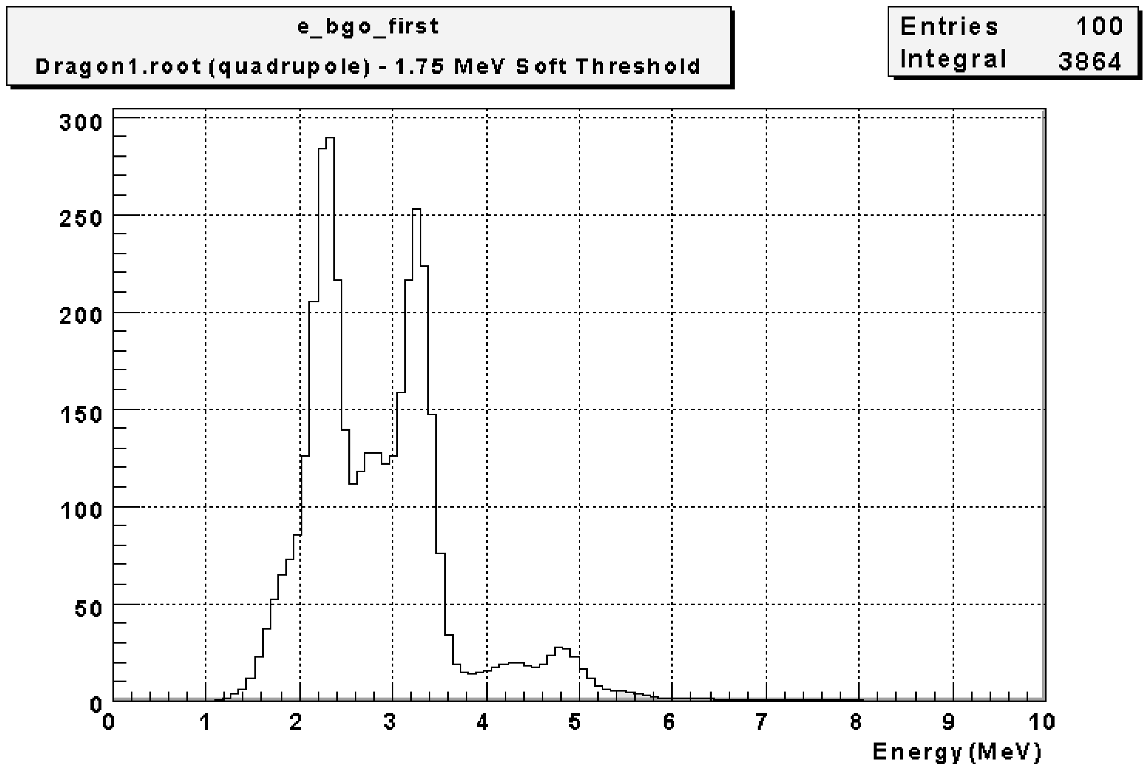

FIGURE 3.6: *Sample first gamma histogram after convolution with gaussian and application of 1.75 MeV shaped threshold (quadrupole angular distribution).*

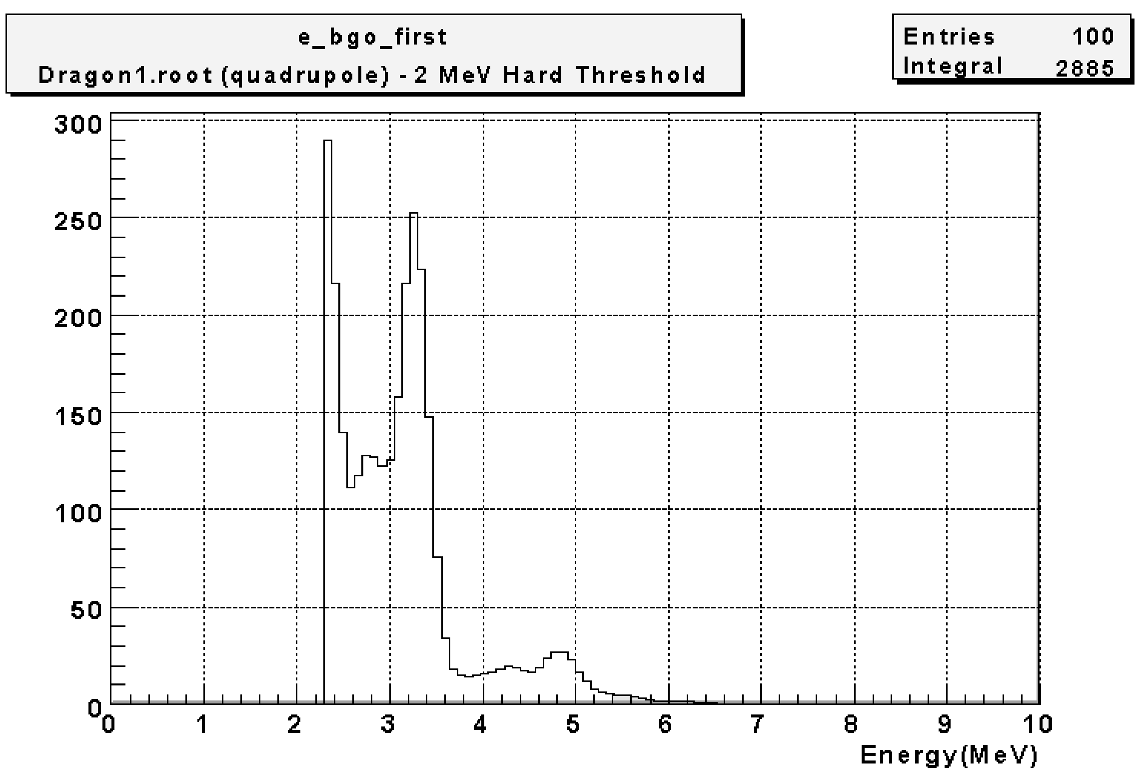

FIGURE 3.7: *Sample first gamma histogram after convolution with gaussian and application of 2 MeV sharp threshold (quadrupole angular distribution).*

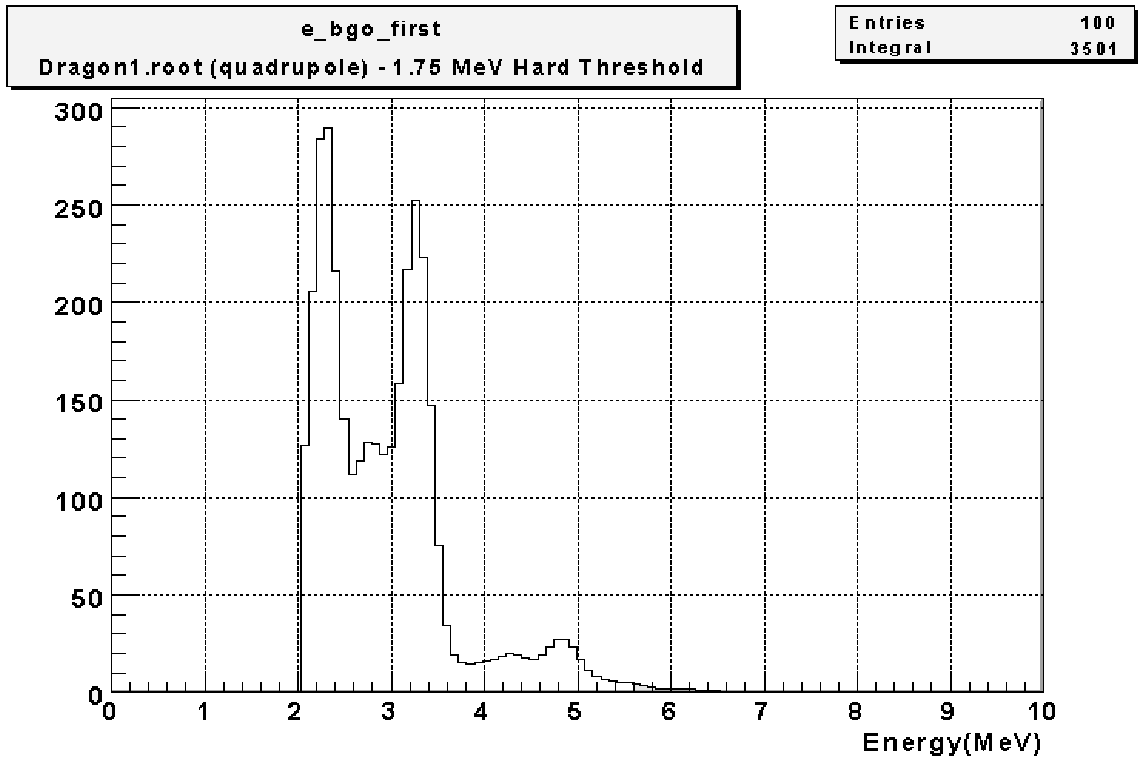

FIGURE 3.8: *Sample first gamma histogram after convolution with gaussian and application of 1.75 MeV sharp threshold (quadrupole angular distribution).*

3.3 EFFICIENCY RESULTS

After convolution of the gamma spectra and application of the various thresholds, BGO efficiencies were calculated by comparing the integral of the first gamma spectrum with the total number of reactions that occurred. The raw integrals and calculated efficiencies for each threshold and angular distribution combination are summarized in table A.6 in appendix A. After determining the efficiencies for each angular distribution and threshold, the values were combined through averaging. The average was taken over all angular distributions, with the standard deviation of the values constituting the error stemming from assuming a specific distribution. For the shaped thresholds, the efficiency was then also averaged over a low, a good and a high threshold fit; the standard deviation of these values was the error attributed to the threshold approximation. Table 3.3 summarizes the averaged calculated BGO efficiencies for the thresholds considered (the systematic percentage error of ± 10.338 % arising from the difference between the simulation and experimental values is not included in these values).

Threshold	Calculated Averaged BGO Efficiency
2 MeV Fit Threshold	(76.36 ± 1.70) %
1.75 MeV Fit Threshold	(81.40 ± 1.63) %
2 MeV Cut Threshold (cut at 2.3 MeV)	(59.30 ± 1.96) %
1.75 MeV Cut Threshold (cut at 2.05 MeV)	(73.46 ± 1.14) %

TABLE 3.3: *Calculated BGO efficiency results for a number of different thresholds.*

In considering the two different energy thresholds that were used in this experiment, the 2 MeV threshold is well-approximated by the gaussian fit which was made to a number of background and calibration runs. Thus, for this energy, use of the fit threshold is appropriate. However, for the 1.75 MeV energy threshold, background and calibration runs did not show an easily approximated threshold, and so a shifted gaussian identical to that used to estimate the 2 MeV threshold was used. While this approach is perhaps justifiable, the more conservative method would be to make use of an energy cut at approximately 2.05 MeV, or the high energy edge of the threshold. While this cut would also have to be made in data analysis, this approach is likely more reliable for the 1.75 MeV threshold level.

Ideally, in determining BGO efficiency, the angular distribution of the gamma radiation should be more accurately known, to eliminate this source of additional error. In fact, work on this aspect of the simulation is currently underway.

4 CONCLUSION

Two important quantities in the calculation of thick target yield, which is used in the determination of resonance strengths for narrow resonance reactions, were investigated for the ^{26g}Al(p,γ)^{27}Si reaction. Beam normalization, or determination of the total number of ^{26g}Al particles on target, was undertaken for over 250 runs. Due to a lack of data for a portion of the runs, two distinct normalization methods were used and refined, utilizing the elastics monitor within the gas target and the current recorded on the left mass slit. These two methods provided validation for one another, providing normalized beam values that agreed within 8%. Calculation of the BGO efficiency using GEANT simulations was also investigated. While these are estimates which attempt to average over a number of possible angular distributions, the efficiencies calculated provide a starting point for future simulations taking into account a more accurate knowledge of the angular distribution of emitted gamma radiation.

5 REFERENCES

[1] C. Rolfs and W. Rodney, **Cauldrons in the Cosmos** (University of Chicago Press, 1988).

[2] National Aeronautics and Space Administration, *www.nasa.gov/vision/universe/starsgalaxies/kepler.html.*

[3] Ruiz, C, **E989: Astrophysical studies using ^{26}Al ground-state and isomer beams**, TRIUMF research proposal (internal), (2004).

[4] D. Hutcheon et al., Nuclear Instruments and Methods in Physics Research A **498**, 190 (2003).

[5] D. Gigliotti, Master's thesis, University of Northern British Columbia, (2003).

[6] C. Wrede, Master’s thesis, Simon Fraser University, (2003).

[7] M. Lamey, Master’s thesis, Simon Fraser University, (2004).

[8] S. Bishop, PhD thesis, Simon Fraser University, (2003).

[9] W. Liu, Master’s thesis, Simon Fraser University, (2001).

[10] C. Galt, TRIUMF DRAGON Summer Report (2003).

APPENDIX A: TABULATED DATA

The following five data tables summarize the beam normalization values obtained from the two methods used for the 250 runs taken over the course of the 3-week experiment. All data contained within this appendix is also compiled within an EXCEL spreadsheet available on ibm00 in home/hcrawfor/Public/26Alpg/Master Run Data.xls. The spreadsheet has also been submitted to the online ELog at https://elog.triumf.ca/Dragon/E989/14.

TABLE A.1: *A run-by-run summary of the calculated values for FC1/FC4 and FC4/Left Mass Slit Current ratios. Yellow and blue runs correspond to low transmission as indicated in section 2.3.*

Run Number	Duration	FC1/FC4	FC4/LeftMassSlit	Run Number	Duration	FC1/FC4	FC4/LeftMassSlit
14843	7085	0.448	0.632	14969	7420	0.532	0.595
14844	162	--	--	14970	7289	0.532	0.571
14845	3841	--	0.646	14971	6680	0.538	0.458
14846	29	--	--	14972	6429	0.517	0.676
14847	6182	0.402	0.626	14973	6677	0.524	0.621
14848	3061	0.500	0.629	14974	7834	0.525	0.588
14849	3151	0.500	0.649	14975	7172	0.502	0.578
14850	5785	0.510	0.575	14976	1273	0.533	0.593
14851	5369	0.510	0.590	14977	7531	0.533	0.526
14852	4175	0.514	0.608	14978	2631	0.544	0.588
14853	693	--	--	14979	167	--	--
14854	7268	0.527	0.552	14980	313	--	--
14855	7159	0.516	0.604	14981	--	--	--
14856	6949	0.558	0.571	14982	354	--	--
14857	73	0.533	--	14983	400	--	--
14858	6952	0.533	0.536	14984	2145	0.455	0.751
14859	7873	0.522	0.613	14985	564	--	--
14860	108	--	--	14986	7214	0.480	0.751
14861	53	--	--	14987	3960	0.462	0.707
14862	8788	0.509	0.614	14988	7081	0.453	0.550
14863	8664	0.500	0.590	14989	7880	0.452	0.672
14864	2340	0.528	0.587	14990	7711	0.469	0.664
14865	7090	0.548	0.540	14991	7189	0.457	0.689
14866	6545	0.513	0.591	14992	7207	0.457	0.723
14867	7610	0.523	0.594	14993	7160	0.467	0.665
14868	79	--	--	14994	1473	0.461	0.658
14869	7210	0.526	0.563	14995	7301	0.453	0.721
14870	6970	0.559	0.558	14996	6594	0.490	0.692
14871	7200	0.538	0.575	14997	476	0.462	0.669
14872	7044	0.535	0.574	14998	1609	--	--
14873	724	--	--	14999	865	--	--
14874	7087	0.474	0.686	15000	195	--	--
14875	7376	0.489	0.613	15001	97	--	--
14876	6600	0.475	0.633	15002	161	--	--
14877	32640	--	--	15003	1036	0.476	0.685
14878	7239	0.517	0.577	15004	--	--	--
14879	7077	0.531	0.576	15005	--	--	--

14880	7167	0.548	0.582	15006	--	--	--
14881	4156	0.533	0.576	15007	--	--	--
14882	167	0.533	0.632	15008	--	--	--
14883	7048	0.525	0.578	15009	1155	0.469	0.667
14884	7175	0.513	0.644	15010	7054	0.469	0.693
14885	--	--	--	15011	7307	0.464	0.586
14886	6991	0.505	0.599	15012	3158	0.478	0.642
14887	2359	0.512	0.591	15013	7201	0.480	0.633
14888	554	--	--	15014	6505	0.481	0.614
14889	7090	0.476	0.651	15015	4977	0.475	0.569
14890	7166	0.505	0.564	15016	--	--	--
14891	35	0.517	0.569	15017	--	--	--
14892	4006	0.514	0.539	15018	7219	0.466	0.666
14893	1097	--	--	15019	7426	0.468	0.643
14894	707	--	--	15020	7093	0.478	0.683
14895	122	--	--	15021	7128	0.475	0.659
14896	220	0.490	0.674	15022	6811	0.495	0.616
14897	7552	0.490	0.631	15023	113	--	--
14898	4909	0.491	0.627	15024	97	--	--
14899	7206	0.500	0.585	15025	102	0.479	0.689
14900	7191	0.522	0.598	15026	457	--	--
14901	7200	0.483	0.649	15027	7510	0.474	0.710
14902	7201	0.508	0.619	15028	7868	0.470	0.685
14903	7854	0.500	0.729	15029	8036	0.468	0.653
14904	7333	0.500	0.559	15030	7201	0.497	0.572
14905	7306	0.529	0.658	15031	7251	0.544	0.556
14906	8235	0.509	0.670	15032	7211	0.542	0.579
14907	7979	0.500	0.658	15033	842	0.549	0.565
14908	7414	0.545	0.328	15034	615	0.510	0.581
14909	7194	0.500	0.612	15035	371	0.544	0.569
14910	7200	0.457	0.592	15036	2111	0.544	0.544
14911	7200	0.496	0.590	15037	2826	0.528	--
14912	7751	0.450	0.694	15038	7447	0.521	0.620
14913	7033	0.580	0.557	15039	6901	0.529	0.598
14914	7066	0.478	0.646	15040	7200	0.522	0.615
14915	11	--	--	15041	7574	0.531	0.646
14916	7243	0.481	0.638	15042	7385	0.516	0.589
14917	7202	0.509	0.658	15043	8470	0.536	0.594
14918	6065	0.485	0.589	15044	7219	0.537	0.606
14919	7241	0.527	0.663	15045	7205	0.515	0.614
14920	941	0.523	--	15046	1207	0.537	0.600
14921	3600	0.495	0.611	15047	7206	0.534	0.621
14922	7202	0.493	0.652	15048	8795	0.519	0.611
14923	7860	0.474	0.690	15049	6746	0.656	0.396
14924	8691	0.519	0.598	15050	898	0.536	0.588
14925	7202	0.480	0.656	15051	226	0.542	0.607
14926	--	0.519	--	15052	367	0.523	0.609
14927	7237	0.405	0.846	15053	334	--	--
14928	3034	0.332	0.958	15054	476	--	--
14929	7146	0.307	0.983	15055	1389	--	--
14930	6897	0.288	1.117	15056	8164	0.502	0.650
14931	1686	0.301	0.961	15057	7312	0.491	0.736

14932	--	0.286	--	15058	6039	0.545	0.591
14933	6840	0.286	0.949	15059	949	0.525	0.627
14934	7220	0.338	0.867	15060	7305	0.527	0.551
14935	7201	0.452	0.698	15061	7201	0.536	0.599
14936	7202	0.233	1.388	15062	7200	0.531	0.616
14937	2716	0.249	1.272	15063	8333	0.537	0.683
14938	750	--	--	15064	8000	0.571	0.509
14939	119	--	--	15065	7305	0.524	0.669
14940	72	--	--	15066	9188	0.526	0.671
14941	51	--	--	15067	11264	0.500	0.750
14942	711	--	--	15068	7335	0.505	0.658
14943	49	--	--	15069	7139	0.516	0.628
14944	--	--	--	15070	7188	0.535	0.610
14945	--	--	--	15071	4453	0.545	0.645
14946	67	--	--	15072	7351	0.526	0.613
14947	351	--	--	15073	8071	0.535	0.644
14948	7884	--	--	15074	7265	0.532	0.639
14949	466	--	--	15075	7229	0.490	0.580
14950	6655	0.357	0.670	15076	7493	0.492	0.707
14951	7223	0.419	0.573	15077	7421	0.411	0.760
14952	7484	0.570	0.519	15078	7465	0.490	0.751
14953	7201	0.525	0.543	15079	3066	0.519	0.636
14954	7200	0.503	0.589	15080	10919	0.482	0.569
14955	7201	0.565	0.522	15081	8762	0.553	0.620
14956	7201	0.552	0.568	15082	9144	0.532	0.642
14957	8165	0.521	0.524	15083	7271	0.527	0.647
14958	8963	0.548	0.530	15084	5068	0.524	0.724
14959	8177	0.434	0.591	15085	7430	0.478	0.672
14960	7864	0.513	--	15086	1030	0.520	--
14961	46	--	--	15087	8713	0.520	0.681
14962	7410	0.503	0.664	15088	884	0.521	0.616
14963	7464	0.517	0.566	15089	10510	--	--
14964	7349	0.520	0.596	15090	9986	0.525	0.625
14965	7492	0.535	0.550	15091	8349	0.517	0.607
14966	7402	0.526	0.586	15092	9398	0.519	0.613
14967	7857	0.517	0.577	15093	8789	0.500	0.588
14968	1085	0.516	0.613	15094	10697	0.525	0.604

TABLE A.2: *A run-by-run summary of the values for integrated left mass slit and normalized beam on target using left mass slit method.*

Run Number	Integrated Left Mass Slit (Coulombs) ($\times 10^{-7}$)	Beam Particles on Target (Left Mass Slit) ($\times 10^{11}$)	Run Number	Integrated Left Mass Slit (Coulombs) ($\times 10^{-7}$)	Beam Particles on Target (Left Mass Slit) ($\times 10^{11}$)
14843	7.66 ± 0.38	4.83 ± 0.24	14969	23.01 ± 1.14	14.52 ± 0.73
14844	0.178 ± 0.009	0.112 ± 0.006	14970	19.38 ± 0.96	12.23 ± 0.61
14845	3.73 ± 0.18	2.35 ± 0.12	14971	17.14 ± 0.85	10.82 ± 0.54
14846	0	0	14972	20.73 ± 1.02	13.08 ± 0.65

14847	8.11 ± 0.40	5.12 ± 0.26
14848	2.59 ± 0.13	1.64 ± 0.08
14849	3.74 ± 0.19	2.36 ± 0.12
14850	8.70 ± 0.43	5.49 ± 0.27
14851	7.72 ± 0.38	4.87 ± 0.24
14852	6.96 ± 0.34	4.39 ± 0.22
14853	1.15 ± 0.06	0.73 ± 0.04
14854	13.82 ± 0.68	8.72 ± 0.44
14855	12.47 ± 0.62	7.87 ± 0.39
14856	11.73 ± 0.58	7.40 ± 0.37
14857	0.037 ± 0.002	0.023 ± 0.001
14858	12.21 ± 0.60	7.70 ± 0.39
14859	13.47 ± 0.67	8.50 ± 0.42
14860	0.232 ± 0.011	0.146 ± 0.007
14861	0.106 ± 0.005	0.067 ± 0.003
14862	15.81 ± 0.78	9.98 ± 0.50
14863	16.39 ± 0.81	10.34 ± 0.52
14864	4.89 ± 0.24	3.08 ± 0.15
14865	13.34 ± 0.66	8.42 ± 0.42
14866	11.93 ± 0.59	7.53 ± 0.38
14867	16.33 ± 0.81	10.30 ± 0.52
14868	0.020 ± 0.001	0.0123 ± 0.0006
14869	16.07 ± 0.79	10.14 ± 0.51
14870	15.49 ± 0.77	9.78 ± 0.49
14871	17.03 ± 0.84	10.75 ± 0.54
14872	16.67 ± 0.82	10.52 ± 0.53
14873	0	0
14874	20.11 ± 0.99	12.69 ± 0.63
14875	21.19 ± 1.05	13.37 ± 0.67
14876	20.12 ± 0.99	12.70 ± 0.63
14877	0	0
14878	70.56 ± 3.49	44.53 ± 2.23
14879	56.67 ± 2.79	35.76 ± 1.79
14880	54.58 ± 2.70	34.44 ± 1.72
14881	32.74 ± 1.62	20.66 ± 1.03
14882	0.920 ± 0.045	0.58 ± 0.03
14883	62.55 ± 3.09	39.48 ± 1.97
14884	46.24 ± 2.28	29.18 ± 1.46
14885	--	--
14886	36.56 ± 1.81	23.07 ± 1.15
14887	15.95 ± 0.79	10.07 ± 0.50
14888	0.160 ± 0.008	0.101 ± 0.005
14889	34.41 ± 1.70	21.71 ± 1.09
14890	45.97 ± 2.27	29.01 ± 1.45
14891	0.213 ± 0.011	0.130 ± 0.007
14892	19.74 ± 0.98	12.45 ± 0.62
14893	0	0
14894	0	0

14973	22.25 ± 1.10	14.04 ± 0.70
14974	24.79 ± 1.22	15.64 ± 0.78
14975	23.96 ± 1.18	15.12 ± 0.76
14976	3.32 ± 0.16	2.10 ± 0.10
14977	30.20 ± 1.49	19.06 ± 0.95
14978	7.96 ± 0.39	5.02 ± 0.25
14979	0.55 ± 0.027	0.35 ± 0.02
14980	0.359 ± 0.018	0.23 ± 0.01
14981	--	--
14982	0.287 ± 0.014	0.181 ± 0.009
14983	0.000	0.000
14984	5.46 ± 0.25	3.79 ± 0.18
14985	--	--
14986	16.98 ± 0.79	11.78 ± 0.57
14987	9.63 ± 0.45	6.68 ± 0.32
14988	19.16 ± 0.89	13.29 ± 0.64
14989	21.53 ± 1.00	14.93 ± 0.72
14990	23.57 ± 1.10	16.35 ± 0.79
14991	19.52 ± 0.91	13.54 ± 0.66
14992	20.18 ± 0.94	14.00 ± 0.68
14993	19.24 ± 0.90	13.34 ± 0.65
14994	3.93 ± 0.18	2.73 ± 0.13
14995	15.21 ± 0.71	10.55 ± 0.51
14996	21.17 ± 0.99	14.68 ± 0.71
14997	1.57 ± 0.07	1.09 ± 0.05
14998	--	--
14999	0.00094 ± 0.00004	0.00066 ± 0.00003
15000	--	--
15001	0.00023 ± 0.00001	0.000159 ± 0.000008
15002	0.00157 ± 0.00007	0.00109 ± 0.00005
15003	3.77 ± 0.18	2.61 ± 0.13
15004	--	--
15005	--	--
15006	--	--
15007	--	--
15008	--	--
15009	4.71 ± 0.22	3.27 ± 0.16
15010	24.95 ± 1.16	17.30 ± 0.84
15011	26.13 ± 1.22	18.12 ± 0.88
15012	9.91 ± 0.46	6.87 ± 0.33
15013	24.80 ± 1.16	17.20 ± 0.83
15014	16.18 ± 0.75	11.22 ± 0.54
15015	21.43 ± 1.00	14.87 ± 0.72
15016	--	--
15017	--	--
15018	25.75 ± 1.20	17.86 ± 0.86
15019	24.86 ± 1.16	17.24 ± 0.83
15020	25.04 ± 1.17	17.37 ± 0.84

14895	0	0
14896	1.60 ± 0.08	1.01 ± 0.05
14897	51.11 ± 2.53	32.26 ± 1.61
14898	38.80 ± 1.92	24.49 ± 1.22
14899	68.63 ± 3.39	43.31 ± 2.16
14900	60.88 ± 3.01	38.41 ± 1.92
14901	66.97 ± 3.31	42.26 ± 2.11
14902	58.22 ± 2.88	36.74 ± 1.84
14903	70.91 ± 3.50	44.75 ± 2.24
14904	71.57 ± 3.54	45.17 ± 2.26
14905	62.19 ± 3.07	39.25 ± 1.96
14906	70.70 ± 3.49	44.62 ± 2.23
14907	63.11 ± 3.12	39.83 ± 1.99
14908	56.10 ± 2.77	35.41 ± 1.77
14909	44.04 ± 2.18	27.79 ± 1.39
14910	37.14 ± 1.83	23.44 ± 1.17
14911	53.07 ± 2.62	33.49 ± 1.67
14912	56.20 ± 2.78	35.46 ± 1.77
14913	54.60 ± 2.70	34.46 ± 1.72
14914	53.63 ± 2.65	33.84 ± 1.69
14915	0.045 ± 0.002	0.028 ± 0.001
14916	53.17 ± 2.63	33.56 ± 1.68
14917	54.61 ± 2.70	34.46 ± 1.72
14918	54.86 ± 2.71	34.62 ± 1.73
14919	53.01 ± 2.62	33.45 ± 1.67
14920	3.17 ± 0.16	2.00 ± 0.10
14921	33.24 ± 1.64	20.98 ± 1.05
14922	64.97 ± 3.21	41.00 ± 2.05
14923	69.68 ± 3.44	43.97 ± 2.20
14924	67.64 ± 3.34	42.69 ± 2.13
14925	51.78 ± 2.56	32.68 ± 1.63
14926	--	--
14927	56.65 ± 2.80	55.41 ± 4.89
14928	19.53 ± 0.97	19.10 ± 1.69
14929	41.85 ± 2.07	40.93 ± 3.61
14930	44.28 ± 2.19	43.31 ± 3.82
14931	11.16 ± 0.55	10.91 ± 0.96
14932	--	--
14933	47.31 ± 2.34	46.28 ± 4.09
14934	75.19 ± 3.71	73.54 ± 6.49
14935	81.52 ± 4.03	79.73 ± 7.04
14936	38.59 ± 1.91	37.74 ± 3.33
14937	17.03 ± 0.84	16.66 ± 1.47
14938	0.032 ± 0.002	0.031 ± 0.003
14939	0.016 ± 0.001	0.016 ± 0.001
14940	0	0
14941	0.0025 ± 0.0001	0.0024 ± 0.0002
14942	--	--
14943	0.00027 ± 0.00001	0.00026 ± 0.00002

15021	24.36 ± 1.14	16.89 ± 0.82
15022	17.96 ± 0.84	12.46 ± 0.60
15023	0.377 ± 0.018	0.26 ± 0.01
15024	0.315 ± 0.015	0.22 ± 0.01
15025	0.318 ± 0.015	0.22 ± 0.01
15026	--	--
15027	21.17 ± 0.99	14.68 ± 0.71
15028	19.39 ± 0.90	13.45 ± 0.65
15029	19.92 ± 0.93	13.82 ± 0.67
15030	20.61 ± 1.02	13.00 ± 0.65
15031	20.26 ± 1.00	12.79 ± 0.64
15032	21.03 ± 1.04	13.27 ± 0.66
15033	2.49 ± 0.12	1.57 ± 0.08
15034	1.54 ± 0.08	0.97 ± 0.05
15035	1.04 ± 0.05	0.66 ± 0.03
15036	1.10 ± 0.05	0.70 ± 0.03
15037	0.032 ± 0.002	0.02 ± 0.001
15038	22.10 ± 1.09	13.95 ± 0.70
15039	19.32 ± 0.95	12.19 ± 0.61
15040	0.70 ± 0.03	0.44 ± 0.02
15041	21.12 ± 1.04	13.33 ± 0.67
15042	18.98 ± 0.94	11.98 ± 0.60
15043	21.45 ± 1.06	13.53 ± 0.68
15044	27.38 ± 1.35	17.28 ± 0.86
15045	17.94 ± 0.89	11.32 ± 0.57
15046	4.01 ± 0.20	2.53 ± 0.12
15047	21.85 ± 1.08	13.79 ± 0.69
15048	29.60 ± 1.46	18.68 ± 0.93
15049	21.98 ± 1.09	13.87 ± 0.69
15050	2.48 ± 0.12	1.56 ± 0.08
15051	0.71 ± 0.04	0.45 ± 0.02
15052	1.17 ± 0.06	0.74 ± 0.04
15053	1.04 ± 0.05	0.66 ± 0.03
15054	1.45 ± 0.07	0.91 ± 0.05
15055	1.68 ± 0.08	1.06 ± 0.05
15056	23.72 ± 1.17	14.97 ± 0.75
15057	26.07 ± 1.29	16.45 ± 0.82
15058	20.39 ± 1.01	12.87 ± 0.64
15059	2.89 ± 0.14	1.82 ± 0.09
15060	24.42 ± 1.21	15.41 ± 0.77
15061	22.77 ± 1.13	14.37 ± 0.72
15062	23.53 ± 1.16	14.85 ± 0.74
15063	26.91 ± 1.33	16.98 ± 0.85
15064	23.86 ± 1.18	15.06 ± 0.75
15065	22.08 ± 1.09	13.93 ± 0.70
15066	28.54 ± 1.41	18.01 ± 0.90
15067	35.22 ± 1.74	22.22 ± 1.11
15068	21.90 ± 1.08	13.82 ± 0.69
15069	19.03 ± 0.94	12.01 ± 0.60

14944	--	--	15070	22.16 ± 1.09	13.98 ± 0.70
14945	--	--	15071	12.66 ± 0.63	7.99 ± 0.40
14946	--	--	15072	21.57 ± 1.07	13.61 ± 0.68
14947	3.41 ± 0.17	3.33 ± 0.29	15073	22.98 ± 1.14	14.50 ± 0.72
14948	71.44 ± 3.53	69.88 ± 6.17	15074	20.38 ± 1.01	12.86 ± 0.64
14949	2.93 ± 0.15	2.87 ± 0.25	15075	18.60 ± 0.92	11.74 ± 0.59
14950	33.31 ± 1.65	32.58 ± 2.88	15076	21.10 ± 1.04	13.32 ± 0.67
14951	11.42 ± 0.56	11.17 ± 0.99	15077	15.45 ± 0.76	9.75 ± 0.49
14952	19.71 ± 0.97	12.44 ± 0.62	15078	18.33 ± 0.91	11.57 ± 0.58
14953	17.79 ± 0.88	11.22 ± 0.56	15079	6.58 ± 0.33	4.15 ± 0.21
14954	17.10 ± 0.85	10.79 ± 0.54	15080	31.95 ± 1.58	20.16 ± 1.01
14955	15.39 ± 0.76	9.71 ± 0.49	15081	24.72 ± 1.22	15.60 ± 0.78
14956	18.72 ± 0.93	11.81 ± 0.59	15082	23.47 ± 1.16	14.81 ± 0.74
14957	17.07 ± 0.84	10.77 ± 0.54	15083	21.34 ± 1.05	13.46 ± 0.67
14958	20.83 ± 1.03	13.14 ± 0.66	15084	13.75 ± 0.68	8.68 ± 0.43
14959	21.37 ± 1.06	13.48 ± 0.67	15085	17.00 ± 0.84	10.73 ± 0.54
14960	14.45 ± 0.71	9.12 ± 0.46	15086	0.026 ± 0.001	0.0167 ± 0.0008
14961	--	--	15087	20.23 ± 1.00	12.76 ± 0.64
14962	23.25 ± 1.15	14.67 ± 0.73	15088	2.68 ± 0.13	1.69 ± 0.08
14963	20.01 ± 0.99	12.62 ± 0.63	15089	27.65 ± 1.37	17.45 ± 0.87
14964	25.41 ± 1.26	16.03 ± 0.80	15090	27.44 ± 1.36	17.32 ± 0.87
14965	32.39 ± 1.60	20.44 ± 1.02	15091	20.45 ± 1.01	12.90 ± 0.64
14966	25.83 ± 1.28	16.30 ± 0.81	15092	18.13 ± 0.90	11.44 ± 0.57
14967	29.99 ± 1.48	18.92 ± 0.95	15093	15.32 ± 0.76	9.67 ± 0.48
14968	3.70 ± 0.18	2.33 ± 0.12	15094	22.93 ± 1.13	14.47 ± 0.72

TABLE A.3: *Calculation of R Values for runs where calculation was possible (stable beam for first 300s & elastics monitor working)*

Run Number	Start FC4 (A)	Elastics (300s)	% Live Time	R
14952	151	5656 ± 75	97.1	1206 ± 98
14954	147	4936 ± 70	97.3	1345 ± 110
14955	131	4848 ± 70	97.2	1219 ± 100
14958	135	5532 ± 74	97	1112 ± 91
14959	175	5552 ± 75	94.9	1402 ± 114
14963	203	7044 ± 84	95.2	1278 ± 104
14964	225	7912 ± 89	94.8	1253 ± 102
14965	243	8764 ± 94	94.5	1215 ± 99
14966	272	9092 ± 95	94.6	1309 ± 106
14967	267	8832 ± 94	94.5	1318 ± 107
14968	217	8808 ± 94	94.7	1071 ± 87
14969	220	7224 ± 85	94.9	1351 ± 110
14970	190	6900 ± 83	95.2	1230 ± 100
14973	210	5552 ± 75	94.4	1676 ± 137
14975	215	7024 ± 84	94.4	1353 ± 110

Run Number	Start FC4 (A)	Elastics (300s)	% Live Time	R
15037	180	6576 ± 81	93	1200 ± 98
15039	170	6184 ± 79	91.7	1208 ± 98
15040	180	6216 ± 79	91.1	1265 ± 103
15041	175	6208 ± 79	91.6	1237 ± 101
15044	259	8872 ± 94	92.3	1294 ± 105
15045	198	7276 ± 85	93.5	1215 ± 99
15046	205	7204 ± 85	92.9	1260 ± 103
15048	212	7220 ± 85	91.7	1281 ± 104
15057	285	8796 ± 94	89.8	1374 ± 112
15058	211	7328 ± 86	89.9	1223 ± 100
15059	200	6304 ± 79	89.9	1348 ± 110
15060	184	6132 ± 78	89.6	1271 ± 104
15061	179	6068 ± 78	89.5	1251 ± 102
15062	207	7136 ± 84	88.9	1221 ± 99
15063	231	7776 ± 88	89.2	1251 ± 102

14976	195	6524 ± 81	94.8	1323 ± 108	15064	140	5552 ± 75	89.8	1068 ± 87
14977	210	7720 ± 88	94.3	1196 ± 97	15065	210	6656 ± 82	90.6	1350 ± 110
14986	198	5436 ± 74	94.4	1607 ± 88	15067	240	6796 ± 82	91.4	1522 ± 124
14987	145	4120 ± 64	94.1	1544 ± 86	15068	198	6348 ± 80	91.7	1354 ± 110
14990	213	5852 ± 76	93.7	1584 ± 87	15069	184	5672 ± 75	92	1409 ± 115
14991	208	6140 ± 78	93.7	1473 ± 81	15070	187	6012 ± 78	91.2	1338 ± 109
14992	210	5552 ± 75	93.8	1643 ± 90	15072	192	6252 ± 79	91.2	1320 ± 108
14993	180	5416 ± 74	93.9	1443 ± 79	15073	202	6488 ± 81	91.3	1341 ± 109
14994	178	5640 ± 75	93.7	1366 ± 75	15074	188	6388 ± 80	91.6	1274 ± 104
14995	190	5132 ± 72	94.1	1608 ± 89	15075	145	4800 ± 69	92.2	1314 ± 108
15010	277	7512 ± 87	91.3	1560 ± 85	15076	183	5940 ± 77	92.5	1346 ± 110
15011	224	6656 ± 82	91	1420 ± 78	15077	180	5036 ± 71	93.1	1571 ± 128
15012	230	6504 ± 81	91.4	1499 ± 82	15078	202	5808 ± 76	93	1525 ± 124
15013	250	7332 ± 86	90.7	1434 ± 78	15079	158	5192 ± 72	93.3	1352 ± 110
15014	210	6264 ± 79	91.8	1421 ± 78	15081	190	6660 ± 82	92.9	1256 ± 102
15018	283	7932 ± 89	89.2	1475 ± 80	15082	188	6252 ± 79	93.1	1325 ± 108
15027	215	6328 ± 80	92	1470 ± 81	15083	188	6396 ± 80	92.6	1287 ± 105
15028	200	6068 ± 78	91.9	1423 ± 78	15086	177	6304 ± 79	92.7	1230 ± 100
15030	169	5732 ± 76	90.5	1253 ± 102	15088	192	6144 ± 78	93.7	1387 ± 113
15035	158	5744 ± 76	91.5	1172 ± 96	15091	180	5916 ± 77	91.6	1322 ± 108
15036	158	6240 ± 79	91.7	1081 ± 88	15094	120	4180 ± 65	93.4	1266 ± 104

TABLE A.4: *A run-by-run summary of the values for normalized beam on target using elastic monitor method for runs where elastic monitor was working correctly.*

Run Number	**Number of Beam Particles on Target (Elastics) (x10^{11})**	**Run Number**	**Number of Beam Particles on Target (Elastics) (x10^{11})**	**Run Number**	**Number of Beam Particles on Target (Elastics) (x10^{11})**
14952	10.73 ± 0.13	14999	0.0026 ± 0.0005	15052	0.71 ± 0.01
14953	9.73 ± 0.12	15000	0.0009 ± 0.0003	15053	0.62 ± 0.01
14954	9.33 ± 0.12	15002	0.0009 ± 0.0003	15054	0.9 ± 0.01
14955	8.48 ± 0.11	15003	2.44 ± 0.04	15055	1 ± 0.02
14956	10.46 ± 0.15	15009	3.18 ± 0.05	15056	14.74 ± 0.18
14957	9.7 ± 0.12	15010	16.48 ± 0.25	15057	16.62 ± 0.21
14958	12.03 ± 0.15	15011	17.19 ± 0.26	15058	12.5 ± 0.16
14959	12.3 ± 0.15	15012	6.45 ± 0.1	15059	1.78 ± 0.03
14960	8.68 ± 0.11	15013	16.45 ± 0.25	15060	14.8 ± 0.18
14961	0.073 ± 0.003	15014	10.72 ± 0.16	15061	14.6 ± 0.2
14962	13.85 ± 0.17	15015	14.36 ± 0.22	15062	15.25 ± 0.19
14963	11.78 ± 0.15	15018	17.53 ± 0.26	15063	16.82 ± 0.22
14964	14.85 ± 0.18	15019	16.74 ± 0.25	15064	14.87 ± 0.18
14965	19.1 ± 0.24	15020	16.97 ± 0.25	15065	13.63 ± 0.17
14966	14.67 ± 0.18	15021	16.63 ± 0.25	15066	17.48 ± 0.22
14967	16.86 ± 0.21	15022	12.12 ± 0.19	15067	21.3 ± 0.26
14968	2.13 ± 0.03	15023	0.264 ± 0.007	15068	13.16 ± 0.17
14969	13.23 ± 0.17	15024	0.209 ± 0.006	15069	11.48 ± 0.14

14970	11.12 ± 0.15
14971	9.85 ± 0.12
14972	12.11 ± 0.15
14973	12.81 ± 0.16
14974	14.31 ± 0.18
14975	13.7 ± 0.17
14976	1.88 ± 0.03
14977	17.31 ± 0.21
14978	4.56 ± 0.06
14979	0.321 ± 0.007
14980	0.025 ± 0.002
14982	0.198 ± 0.005
14984	4.15 ± 0.06
14986	11.6 ± 0.17
14987	6.68 ± 0.1
14988	12.77 ± 0.19
14989	14.24 ± 0.21
14990	15.86 ± 0.24
14991	13.26 ± 0.2
14992	13.7 ± 0.21
14993	13.32 ± 0.2
14994	2.74 ± 0.04
14995	10.5 ± 0.16
14996	14.37 ± 0.22
14997	1.01 ± 0.02
14998	0.0012 ± 0.0004

15025	0.183 ± 0.005
15027	15.13 ± 0.23
15028	14.99 ± 0.22
15029	14.39 ± 0.22
15030	12.25 ± 0.15
15031	12.18 ± 0.15
15032	12.72 ± 0.16
15034	0.93 ± 0.01
15035	0.62 ± 0.01
15036	2.8 ± 0.05
15037	5.05 ± 0.07
15038	13.92 ± 0.17
15039	12.33 ± 0.15
15040	13.44 ± 0.17
15041	13.66 ± 0.17
15042	12.52 ± 0.16
15043	13.93 ± 0.17
15044	17.06 ± 0.21
15045	11.39 ± 0.15
15046	2.55 ± 0.03
15047	14 ± 0.17
15048	18.91 ± 0.23
15049	13.99 ± 0.17
15050	1.6 ± 0.02
15051	0.461 ± 0.009

15070	13.43 ± 0.17
15071	7.8 ± 0.1
15072	13.47 ± 0.17
15073	14.41 ± 0.18
15074	12.87 ± 0.18
15075	11.53 ± 0.14
15076	12.93 ± 0.16
15077	10.8 ± 0.13
15078	11.04 ± 0.14
15079	3.95 ± 0.05
15080	19.31 ± 0.24
15081	15.1 ± 0.19
15082	14.4 ± 0.18
15083	13.24 ± 0.16
15084	8.52 ± 0.11
15085	10.56 ± 0.13
15086	1.64 ± 0.02
15087	12.28 ± 0.17
15088	1.58 ± 0.02
15089	16.53 ± 0.2
15090	16.72 ± 0.21
15091	12.9 ± 0.16
15092	11.6 ± 0.14
15093	9.33 ± 0.12
15094	14.61 ± 0.18

TABLE A.5: *A run-by-run summary of the net ^{26g}Al particles on target, after subtraction of ^{26}Na and ^{26m}Al beam contaminants. Values are calculated using beam particles on target calculated by elastic monitor method where possible; where this is not possible beam particles on target as determined using left mass slit method is used.*

Run Number	Net ^{26g}Al Particles on Target
14843	4.80 ± 0.24
14844	0.112 ± 0.006
14845	2.34 ± 0.12
14846	--
14847	5.09 ± 0.26
14848	1.63 ± 0.08
14849	2.35 ± 0.12
14850	5.47 ± 0.27
14851	4.86 ± 0.24
14852	4.38 ± 0.22
14853	0.72 ± 0.04

Run Number	Net ^{26g}Al Particles on Target
14927	55.37 ± 4.89
14928	19.09 ± 1.69
14929	40.89 ± 3.61
14930	43.27 ± 3.82
14931	10.90 ± 0.96
14932	--
14933	46.25 ± 4.08
14934	73.51 ± 6.49
14935	79.70 ± 7.04
14936	37.73 ± 3.33
14937	16.65 ± 1.47

Run Number	Net ^{26g}Al Particles on Target
15011	17.09 ± 0.26
15012	6.41 ± 0.10
15013	16.36 ± 0.25
15014	10.66 ± 0.16
15015	14.28 ± 0.22
15016	--
15017	--
15018	17.43 ± 0.26
15019	16.64 ± 0.25
15020	16.87 ± 0.25
15021	16.54 ± 0.25

14854	8.70 ± 0.44
14855	7.84 ± 0.39
14856	7.38 ± 0.37
14857	0.020 ± 0.001
14858	7.68 ± 0.38
14859	8.48 ± 0.42
14860	0.150 ± 0.007
14861	0.067 ± 0.003
14862	9.95 ± 0.50
14863	10.32 ± 0.52
14864	3.08 ± 0.15
14865	8.40 ± 0.42
14866	7.51 ± 0.38
14867	10.28 ± 0.51
14868	0.0123 ± 0.0006
14869	10.12 ± 0.51
14870	9.76 ± 0.49
14871	10.72 ± 0.54
14872	10.5 ± 0.53
14873	--
14874	12.69 ± 0.63
14875	13.37 ± 0.67
14876	12.70 ± 0.63
14877	--
14878	44.47 ± 2.22
14879	35.72 ± 1.79
14880	34.41 ± 1.72
14881	20.64 ± 1.03
14882	0.58 ± 0.03
14883	39.43 ± 1.97
14884	29.15 ± 1.46
14885	--
14886	23.05 ± 1.15
14887	10.06 ± 0.50
14888	0.101 ± 0.005
14889	21.69 ± 1.08
14890	28.96 ± 1.45
14891	0.134 ± 0.007
14892	12.43 ± 0.62
14893	--
14894	--
14895	--
14896	1.01 ± 0.05
14897	32.26 ± 1.61
14898	24.49 ± 1.22
14899	43.24 ± 2.16
14900	38.35 ± 1.92
14901	42.19 ± 2.11

14938	0.031 ± 0.003
14939	0.016 ± 0.001
14940	--
14941	0.0024 ± 0.0002
14942	--
14943	0.00026 ± 0.00002
14944	--
14945	--
14946	--
14947	3.33 ± 0.29
14948	69.88 ± 6.17
14949	2.87 ± 0.25
14950	32.57 ± 2.88
14951	11.14 ± 0.99
14952	10.69 ± 0.13
14953	9.70 ± 0.12
14954	9.30 ± 0.12
14955	8.45 ± 0.11
14956	10.42 ± 0.15
14957	9.67 ± 0.12
14958	11.98 ± 0.15
14959	12.22 ± 0.15
14960	8.62 ± 0.11
14961	0.073 ± 0.003
14962	13.77 ± 0.17
14963	11.71 ± 0.15
14964	14.76 ± 0.18
14965	19.00 ± 0.24
14966	14.58 ± 0.18
14967	16.76 ± 0.21
14968	2.12 ± 0.03
14969	13.16 ± 0.17
14970	11.04 ± 0.15
14971	9.77 ± 0.12
14972	12.02 ± 0.15
14973	12.72 ± 0.16
14974	14.20 ± 0.18
14975	13.60 ± 0.17
14976	1.87 ± 0.03
14977	17.19 ± 0.21
14978	4.53 ± 0.06
14979	0.320 ± 0.007
14980	0.025 ± 0.002
14981	--
14982	0.197 ± 0.005
14983	--
14984	4.13 ± 0.06
14985	--

15022	12.05 ± 0.19
15023	0.263 ± 0.007
15024	0.207 ± 0.006
15025	0.182 ± 0.005
15026	--
15027	15.05 ± 0.23
15028	14.90 ± 0.22
15029	14.31 ± 0.22
15030	12.14 ± 0.15
15031	12.09 ± 0.15
15032	12.63 ± 0.16
15033	1.57 ± 0.08
15034	0.93 ± 0.01
15035	0.62 ± 0.01
15036	2.79 ± 0.05
15037	5.05 ± 0.07
15038	13.84 ± 0.17
15039	12.26 ± 0.15
15040	13.36 ± 0.17
15041	13.58 ± 0.17
15042	12.45 ± 0.16
15043	13.86 ± 0.17
15044	16.98 ± 0.21
15045	11.33 ± 0.15
15046	2.54 ± 0.03
15047	13.93 ± 0.17
15048	18.8 ± 0.24
15049	13.91 ± 0.17
15050	1.59 ± 0.02
15051	0.458 ± 0.009
15052	0.70 ± 0.01
15053	0.62 ± 0.01
15054	0.90 ± 0.01
15055	0.99 ± 0.02
15056	14.64 ± 0.18
15057	16.50 ± 0.21
15058	12.41 ± 0.16
15059	1.76 ± 0.03
15060	14.68 ± 0.18
15061	14.49 ± 0.20
15062	15.13 ± 0.19
15063	16.68 ± 0.22
15064	14.75 ± 0.18
15065	13.52 ± 0.17
15066	17.35 ± 0.22
15067	21.14 ± 0.26
15068	13.06 ± 0.17
15069	11.39 ± 0.14

14902	36.68 ± 1.83	14986	11.52 ± 0.17	15070	13.32 ± 0.17
14903	44.68 ± 2.23	14987	6.63 ± 0.10	15071	7.74 ± 0.10
14904	45.11 ± 2.26	14988	12.69 ± 0.19	15072	13.38 ± 0.17
14905	39.20 ± 1.96	14989	14.14 ± 0.21	15073	14.30 ± 0.18
14906	44.57 ± 2.23	14990	15.76 ± 0.24	15074	12.79 ± 0.18
14907	39.76 ± 1.99	14991	13.18 ± 0.20	15075	11.43 ± 0.14
14908	35.35 ± 1.77	14992	13.62 ± 0.21	15076	12.82 ± 0.16
14909	27.75 ± 1.39	14993	13.23 ± 0.20	15077	10.72 ± 0.14
14910	23.40 ± 1.17	14994	2.72 ± 0.04	15078	10.94 ± 0.14
14911	33.44 ± 1.67	14995	10.44 ± 0.16	15079	3.91 ± 0.05
14912	35.41 ± 1.77	14996	14.28 ± 0.22	15080	19.16 ± 0.24
14913	34.42 ± 1.72	14997	1.01 ± 0.02	15081	14.98 ± 0.19
14914	33.80 ± 1.69	14998	0.0012 ± 0.0004	15082	14.27 ± 0.18
14915	0.028 ± 0.001	14999	0.0026 ± 0.0005	15083	13.14 ± 0.16
14916	33.52 ± 1.68	15000	0.0009 ± 0.0003	15084	8.46 ± 0.11
14917	34.42 ± 1.72	15001	0.000157 ± 0.000008	15085	10.48 ± 0.13
14918	34.59 ± 1.73	15002	0.0009 ± 0.0003	15086	1.64 ± 0.02
14919	33.41 ± 1.67	15003	2.43 ± 0.04	15087	12.19 ± 0.17
14920	2.00 ± 0.10	15004	--	15088	1.57 ± 0.02
14921	20.96 ± 1.05	15005	--	15089	16.41 ± 0.2
14922	40.95 ± 2.05	15006	--	15090	16.57 ± 0.21
14923	43.91 ± 2.20	15007	--	15091	12.78 ± 0.16
14924	42.64 ± 2.13	15008	--	15092	11.49 ± 0.15
14925	32.63 ± 1.63	15009	3.17 ± 0.05	15093	9.24 ± 0.12
14926	--	15010	16.39 ± 0.25	15094	14.49 ± 0.18

TABLE A.6: *Summary of calculated BGO array efficiency values.*

			Isotropic (L=0)	Dipole (L=1)	Quadrupole (L=2)	Efficiency Averaged Over All Angular Distributions
Total Number of Reactions:			4710 ± 69	4707 ± 69	4711 ± 69	--
2 MeV Fit Threshold	**High Threshold (Mean = 229, Sigma = 0.30)**	**Number of Gammas:**	3488 ± 59	3569 ± 60	3594 ± 60	--
		Efficiency:	(74.06 ± 1.25) %	(75.83 ± 1.27) %	(76.29 ± 1.27) %	(75.39 ± 1.17) %
	'Good' Threshold (Mean = 229, Sigma = 0.33)	**Number of Gammas:**	3535 ± 59	3616 ± 60	3637 ± 60	--
		Efficiency:	(75.06 ± 1.26) %	(76.81 ± 1.28) %	(77.21 ± 1.28) %	(76.36 ± 1.14) %
	Low Threshold (Mean = 229, Sigma = 0.39)	**Number of Gammas:**	3604 ± 60	3682 ± 61	3700 ± 61	--
		Efficiency:	(76.52 ± 1.27) %	(78.22 ± 1.29) %	(78.54 ± 1.29) %	(77.76 ± 1.09) %
	Averaged Efficiency:					(76.36 ± 1.70) %
1.75 MeV Fit Threshold	**High Threshold (Mean = 205, Sigma = 0.30)**	**Number of Gammas:**	3745 ± 61	3822 ± 62	3831 ± 62	--
		Efficiency:	(79.52 ± 1.30) %	(81.20 ± 1.31) %	(81.32 ± 1.31) %	(80.68 ± 1.01) %
	'Good' Threshold (Mean = 205, Sigma = 0.33)	**Number of Gammas:**	3781 ± 61	3855 ± 62	3864 ± 62	--
		Efficiency:	(80.28 ± 1.31) %	(81.91 ± 1.32) %	(82.01 ± 1.32) %	(81.40 ± 0.97) %
	Low Threshold (Mean = 205, Sigma = 0.39)	**Number of Gammas:**	3833 ± 62	3903 ± 62	3910 ± 63	--
		Efficiency:	(81.39 ± 1.31) %	(82.93 ± 1.33) %	(83.00 ± 1.33) %	(82.44 ± 0.91) %
	Averaged Efficiency:					(81.40 ± 1.63) %
2.0 MeV Cut Threshold (cut at 2.3 MeV)	**Number of Gammas:**		2699 ± 52	2794 ± 53	2884 ± 54	--
	Efficiency:		(57.31 ± 1.10) %	(59.36 ± 1.12) %	(61.23 ± 1.14) %	(59.30 ± 1.96) %
1.75 MeV Cut Threshold (cut at 2.05 MeV)	**Number of Gammas:**		3399± 58	3479 ± 59	3501 ± 59	--
	Efficiency:		(72.16 ± 1.24) %	(73.90 ± 1.25) %	(74.31 ± 1.26) %	(73.46 ± 1.14) %

APPENDIX B: SAMPLE CODE

All code can also be found on IBM00 at home/hcrawfor/Public/Macros.

B.1 COMMAND LINE CODE FOR EXTRACTION OF HISTORY DATA

While logged on to the isdaq04 server, and within the experiment folder, the following command line code retrieves data from the history files recorded by MIDAS, where the italics refer to required input fields.

```
[dragon@isdaq04]/data2/dragon/E989>> mhist –e EventID –v Variable Name –s Start
Date (YYMMDD.HHMM) –p End Data (YYMMDD.HHMM)
```

For example,

```
[dragon@isdaq04]/data2/dragon/E989>> mhist –e 20 –v MassSlitLeft –s 050701.0900
–p 050702.0900
```

This code extracts, from event ID 20, which refers to EPICS events, the value of the variable ‘Mass Slit Left’ from July 1, 2005 at 9 am until July 2, 2005 at 9 am.

B.2 ROOT MACRO FOR EXTRACTION OF ELASTICS INTEGRAL FROM .ROOT RUN FILES

```
//
// Automatic SB0 integral extraction from Dragon runs.
// BW June 30'05
//

{
  for (UInt_t i=14843; i<=15094; i++){
    char myfilename[50];
    sprintf(myfilename, "/data2/dragon/E989/his%d.root", i);

    TFile *myFile = new TFile(myfilename);
    if (myFile->IsOpen()){
      TObject *myFolders[4];
      myFolders[0] = myFile->GetObjectUnchecked("histos");
      myFolders[1] = myFolders[0]->FindObject("DragonEvent");
      myFolders[2] = myFolders[1]->FindObject("Singles");
      myFolders[3] = myFolders[2]->FindObject("SbSingles");
      TH2F *myHist = (TH2F *)myFolders[3]->FindObject("hsSbE");
      cout << "file=" << myFile->GetName() << endl;
      cout << "integral=" << myHist->Integral(350, 550, 0, 1) << endl;
      cout << endl;
      if (myFile) delete myFile;
    }
  }
}
```

B.3 ROOT MACRO FOR HPGE ENERGY CALIBRATION

```
//
// Macro to read in HPGe Energy Data and fit a polynomial to the data to
// produce an energy calibration plot.
//
// HCrawford - June 2005 (adapted from macro from C. Ruiz)
//

void energycalib(const char *filename = 0, float N = 5){
  const char *fName = filename;
  Float_t x, y, z;
  int precount = 0;
  ifstream in;

  //
  // Get file data
  //

  cout << "Given data file " << fName << endl
       << "Parameters: N (order of polynomial) = " << N << endl;
  in.open(fName);
  if (in.is_open()) {
    while (! in.eof()) {
      in >> x >> y >> z;

      //
      // Last read from file sets badbit, and x, y, z stay unchanged making
      // it look like we read the last line twice - the following gets round it
      //

      if (in.good()) {
       precount++;
       cout << " = " << x << ",\ty = " << y << ",\tz = " << z << endl;
      }
    }
    cout << "Found " << precount << " lines in data file" << endl;

    //
    // Reset ifstream
    //

    in.clear(ios::goodbit);
    in.seekg(0,ios::beg);
    if (precount>0){
      Int_t n = precount;
      Int_t nlines = 0;

      //
      // Create dynamic arrays
      //

      Float_t *channel = new Float_t[n];
      Float_t *energy = new Float_t[n];
      Float_t *ex = new Float_t[n];
      Float_t *ey = new Float_t[n];

      while (! in.eof()) {
       in >> x >> y >> z;
       if (in.good()) {
         channel[nlines] = x;
         energy[nlines] = y;
         ex[nlines] = z;
```

```
        ey[nlines] = 0;
        nlines++;

        // cout << x << y << z << endl;

      }
     }
    }
    in.close();
  } else {

    //
    // Print error _and_ return if we can't get the data
    //

    cerr << "Could not open file " << fName << endl;
    cout << "Format of data file should be:" << endl
        << "Channel Number, Gamma Energy (keV), Peak Width (sigma)" << endl;
    return;
  }


  //
  // Now, we make sure N is within the allowed range.
  //

  for (;N < 1;){
    cout << "N must be between 1 and 6." << endl;
    return;
  }
  for (;N > 6;){
    cout << "N must be between 1 and 6." << endl;
    return;
  }

  //
  // Now, we make a canvas.
  //

  TCanvas *c1 = new TCanvas("c1" ,"HPGe Energy Calibration graph", 200, 10, 700,
500);
  c1->SetFillColor(19);
  c1->SetGrid();

  //
  // Now for the graph
  //

  TGraphErrors *gr = new TGraphErrors(n, channel, energy, ex, ey);
  gr->SetTitle("HPGe Energy Calibration");
  gr->SetMarkerColor(4);
  gr->SetMarkerStyle(21);
  gr->Draw("ALP");
  gr->GetXaxis()->SetTitle("Channel Number");
  gr->GetXaxis()->CenterTitle();
  gr->GetYaxis()->SetTitle("Gamma Energy (keV)");
  gr->GetYaxis()->SetTitleOffset(1.3);
  gr->GetYaxis()->CenterTitle();

  //
  // Fit appropriate polynomial & get parameters.
  //
```

```
  TF1 *fit = new TF1("fit", "pol1", 0, channel[nlines]);
  gr->Fit("fit","F");
  double intercept = fit->GetParameter(0);
  double slope = fit->GetParameter(1);

  if (N == 1)
    {
      Double_t par[2];
      TF1 *fitFcn = new TF1("fitFcn", "pol1", 0, channel[nlines]);
    }
  else if (N == 2)
    {
      Double_t par[3];
      TF1 *fitFcn = new TF1("fitFcn", "pol2", 0, channel[nlines]);
      }
  else if (N == 3)
    {
      Double_t par[4];
      TF1 *fitFcn = new TF1("fitFcn", "pol3", 0, channel[nlines]);
    }
  else if (N == 4)
    {
      Double_t par[5];
      TF1 *fitFcn = new TF1("fitFcn", "pol4", 0, channel[nlines]);
    }
  else if (N == 5)
    {
      Double_t par[6];
      TF1 *fitFcn = new TF1("fitFcn", "pol5", 0, channel[nlines]);
    }
  else
    {
      Double_t par[7];
      TF1 *fitFcn = new TF1("fitFcn", "pol6", 0, channel[nlines]);
    }

  fitFcn->SetLineColor(kMagenta);
  gr->Fit("fitFcn","F");
  fitFcn->GetParameters(par);
  cout << "Fit parameters:" << endl;
  int i;
  for(int i=0; i <= N; i++)
    {
      par[i]=fitFcn->GetParameter(i);
      cout  << "  par[" << i << "] = " << par[i] << endl;
    }

  //
  // Now, for the legend...
  //

  TLegend *legend = new TLegend(0.15, 0.82, 0.55, 0.87);
  legend->SetTextFont(72);
  legend->SetTextSize(0.04);
  legend->AddEntry(fitFcn, "HPGe Energy Calibration", "l");
  legend->Draw();

  c1->Update();
  c1->GetFrame()->SetFillColor(18);
  c1->GetFrame()->SetBorderSize(6);
  gStyle->SetOptFit();
  c1->Draw();
}
```

B.4 ROOT Macro for HPGe Efficiency Calibration

```
//
// Macro to read in HPGe absolute efficiency data and fit a linear
// polynomial to the data.
//
// HCrawford - June 2005 (adapted from macro from C. Ruiz)
//

//
// void efficiencycalib(const Char_t *filename = 0){
//

void efficiencycalib(const char *filename = 0){
  const char *fName = filename;
  Float_t x, y, z;
  int precount = 0;
  ifstream in;

  //
  // Get file data
  //

  cout << "Given data file " << fName << endl
       << "Parameters: N (order of polynomial) = " << N << endl;
  in.open(fName);
  if (in.is_open()) {
    while (! in.eof()) {
      in >> x >> y >> z;

      //
      // Last read from file sets badbit, and x, y, z stay unchanged making
      // it look like we read the last line twice - the following gets round it
      //

      if (in.good()) {
       precount++;
       cout << " = " << x << ",\ty = " << y << ",\tz = " << z << endl;
      }
    }
    cout << "Found " << precount << " lines in data file" << endl;

    //
    // Reset ifstream
    //

    in.clear(ios::goodbit);
    in.seekg(0,ios::beg);
    if (precount>0){
      Int_t n = precount;
      Int_t nlines = 0;

      //
      // Create dynamic arrays
      //

      Float_t *Energy = new Float_t[n];
      Float_t *Efficiency = new Float_t[n];
      Float_t *ex = new Float_t[n];
      Float_t *ey = new Float_t[n];

      while (! in.eof()) {
       in >> x >> y >> z;
```

```
      if (in.good()) {
        Energy[nlines] = log(x);
        Efficiency[nlines] = log(y);
        ex[nlines] = 0.;
        ey[nlines] = z/y;
        nlines++;

        // cout << x << y << z << endl;

      }
     }
    }
    in.close();
  } else {

    //
    // Print error _and_ return if we can't get the data
    //

    cerr << "Could not open file " << fName << endl;
    cout << "Format of data file should be:" << endl
        << "Gamma Energy (keV), Efficiency, Error in Efficiency" << endl;
    return;
  }

  //
  // Now, we make a canvas.
  //

  TCanvas *c1 = new TCanvas("c1" ,"HPGe Efficiency Calibration graph", 200, 10,
700, 500);
  c1->SetFillColor(19);
  c1->SetGrid();

  //
  // Now for the graph
  //

  TGraphErrors *gr = new TGraphErrors(n, Energy, Efficiency, ex, ey);
  gr->SetTitle("HPGe Efficiency Calibration");
  gr->SetMarkerColor(4);
  gr->SetMarkerStyle(21);
  gr->Draw("ALP");
  gr->GetXaxis()->SetTitle("ln(Gamma Energy in keV)");
  gr->GetXaxis()->CenterTitle();
  gr->GetYaxis()->SetTitle("ln(Efficiency)");
  gr->GetYaxis()->SetTitleOffset(1.3);
  gr->GetYaxis()->CenterTitle();

  //
  // Fit function & get parameters.
  //

  Double_t par[2];
  TF1 *fitFcn = new TF1("fitFcn", "pol1", 0, Energy[nlines]);
  fitFcn->SetLineColor(kMagenta);
  gr->Fit("fitFcn", "F");
  fitFcn->GetParameters(par);
  cout << "Fit parameters:" <<endl;
  par[0]=fitFcn->GetParameter(0);
  par[1]=fitFcn->GetParameter(1);
  cout << "par[0] = " << par[0] << " and par[1] = " << par[1] << endl;
```

```
  //
  // Now for the legend...
  //

  TLegend *legend = new TLegend(0.15, 0.22, 0.60, 0.27);
  legend->SetTextFont(72);
  legend->SetTextSize(0.04);
  legend->AddEntry(fitFcn, "HPGe Efficiency Calibration", "l");
  legend->Draw();

  c1->Update();
  c1->GetFrame()->SetFillColor(18);
  c1->GetFrame()->SetBorderSize(6);
  gStyle->SetOptFit();
  c1->Draw();
}
```

B.5 Sample GEANT Simulation Input Files

B.5.1 26Al(p,γ) Input Data File

```
# Input namelist for 26gAl(p,g)27Si reaction
#  C.Ruiz 22.07.2003
# Note: All mass excesses in GeV
#       All widths in MeV
#       All elevels in MeV
 $params
  life = 15*1000.
  level = 15*0.
  beamtyp = '26Al'
  rectyp = '27Si'
  zbeam = 13.
  abeam = 26.
  atarg = 1.
  ztarg = 1.
  zprod = 14.
  beamlifetime = 1000.
  beam_mass_excess = -12210.31E-06
  recoil_mass_excess = -12384.30E-06
  resenerg = 0.188
  part_width = 0.0001
  gam_width = 0.000001
  spin_stat_fac = 0.136
  ell = 2.
  rstate = 8
  level( 0) = 0.0
  level( 1) = 0.781
  level( 2) = 0.957
  level( 3) = 2.164
  level( 4) = 2.647
  level( 5) = 2.866
  level( 6) = 2.910
  level( 7) = 4.448
  level( 8) = 7.653
  life( 0) = 1000.
  life( 1) = 35.0E-12
  life( 2) = 1.2E-12
  life( 3) = 44.0E-15
  life( 4) = 17.0E-15
  life( 5) = 3.0E-15
  life( 6) = 52.0E-15
  life( 7) = 390.0E-15
```

```
  br(1,1) = 100.
  md(1,1) = 0
  br(2,1) = 94.0
  md(2,1) = 1
  br(2,2) = 6.0
  md(2,2) = 0
  br(3,1) = 100.
  md(3,1) = 0
  br(4,1) = 77.0
  md(4,1) = 2
  br(4,2) = 20.0
  md(4,2) = 0
  br(4,3) = 3.0
  md(4,3) = 1
  br(5,1) = 96.0
  md(5,1) = 0
  br(5,2) = 4.0
  md(5,2) = 1
  br(6,1) = 94.0
  md(6,1) = 0
  br(6,2) = 6.0
  md(6,2) = 3
  br(7,1) = 89.0
  md(7,1) = 3
  br(7,2) = 11.0
  md(7,2) = 6
  br(8,1) = 90.0
  md(8,1) = 7
  br(8,2) = 10.0
  md(8,2) = 6
$[end]
```

B.5.2 ANGULAR DISTRIBUTION INPUT DATA FILE

```
C----67---- gamma angular distribution

      REAL FUNCTION angdist(X)

      REAL pi
      Parameter (pi = 3.1415926)

C     A uniform angular distribution for gammas
      angdist = 1
C     A dipole angular distribution for gammas
C      angdist = (3./(8.*pi))*(1.-X**2)
C     A quad. angular distribution for gammas
C      angdist = (15./(8.*pi))*(1.-X**2)*X**2


      END
```

B.6 GAUSSIAN CONVOLUTION CODE FOR APPROXIMATION OF DETECTOR RESOLUTION

```
//
// Program to convolve BGO data from GEANT to account for detector resolution.
//
// August 8, 2005 -- HCrawford
//

#include<fstream>
#include<iostream>
#include<string>
using namespace std;

//
// Function to define and evaluate required Gaussian at each point.
// Defines sigma from formula FWHM = k*sqrt(E). Calculates and
// returns the convolved value.
//

float gaus(float energy[], int counts[], int j){

  float factor = sqrt(8.0*log(2.0));
  float k = 0.1733;
  float pi = 3.14159265;
  float sigma = (k*sqrt(energy[j]))/factor;
  float calcGaus[100];
  float sum=0.0;

  for (int i=0; i<=99; i++){
    calcGaus[i] = 0;
  }

  for (int i=0; i<=99; i++){
    calcGaus[i]=(0.085/(sqrt(2*pi*sigma*sigma)))*(exp(-((energy[i]-
energy[j])*(energy[i]-energy[j]))/(2*sigma*sigma)));
  }

  for (int i=0; i<=99; i++){
    sum = sum + calcGaus[i]*counts[i];
  }

  return sum;

}

int main (){

  //
  // Acquire input data file name from user and open.
  //

  string name;

  cout << "Enter data file containing BGO data in form Bin# | #Counts: ";
  cin >> name;

  ifstream file;
  file.open(name.c_str(),ios::in);

  //
  // Define necessary variables and arrays, and initialize values.
  //
```

```
int n = 100;
int i = 1;
int bin[n];
bin[0] = 1;
int tempBin;
int tempCounts;
int counts[n];
counts[0] = 0;
int nlines = 0;
float sum = 0.0;
float sumRaw = 0.0;

float energies[n];
energies[0]=0.0425;
for (int i=1; i<=99; i++){
  energies[i] = energies[i-1] + 0.085;
}

float convolution[n];

for (int i=0; i<=99; i++){
  convolution[i]=0;
}

//
// Read in raw data from user-defined input file, if file is opened properly.
//

if(file.is_open()){
  while(! file.eof()){
    file >> tempBin >> tempCounts;

    //
    // This bit of code avoids reading in the last line twice.
    //

    if (file.good()){
     bin[i] = tempBin;
     counts[i] = tempCounts;
     cout << "Bin #" << bin[i] << " contains " << counts[i] << " counts." <<
endl;
     i++;
     nlines++;
    }
  }

  cout << "Found " << nlines << " lines of data in file." << endl;

  //
  // If file is not open, output error message and end program.
  //

}else{
  cout << "The requested file: " << name << ", could not be opened." << endl;
  return 0;
}

//
// For each bin, call gaus function to set required Gaussian and calculate
// the required values, returning the convolution value.
//

for (int i=0; i<=99; i++){
```

```
    convolution[i] = gaus(energies, counts, i);
  }

  //
  // Normalize the convolution values to ensure that the integral is unchanged.
  //

  for (int i=0; i<=99; i++){
    sum = sum + convolution[i];
    sumRaw = sumRaw + counts[i];
  }

  for (int i=0; i<=99; i++){
    convolution[i] = convolution[i]*(sumRaw/sum);
  }

  //
  // Read in a file name from the user, and open this file as the output file.
  //

  string outname;

  cout << "Enter an output file name: ";
  cin >> outname;

  ofstream outfile;
  outfile.open(outname.c_str(),ios::out);

  //
  // Output the convolution values to the indicated file.
  //

  for (int i=0; i<=99; i++){
    outfile << convolution[i] << endl;
  }

  cout << "Convolution complete... output written to " << outname
       << ".  Have a nice day." << endl;

  file.close();
  outfile.close();

  return 0;
}
```

Appendix C: Error Analysis

Standard Formulae Used in Calculation of Averages and Error Propagation

For calculation of average values, the following standard formula was used, where x represents an individual data point in the group of data points being averaged.

$$Average(\bar{x}) = \frac{\sum x}{\#Values} \tag{B.1}$$

Similarly, the following formula was used to calculate the standard deviation of a set of data values, where N is the number of values in the data set.

$$S\tan dardDeviation = \sqrt{\frac{(x-\bar{x})^2}{N-1}} \tag{B.2}$$

The error on the mean was calculated according to the following formula, where once again, N is the number of values in the data set, and σ is the standard deviation of the values in the data set.

$$ErrorOnMean = \frac{\sigma}{\sqrt{N}} \tag{B.3}$$

Weighted averages were calculated according to the following formula, where σ is the error on each individual x value.

$$WeightedAverage = \frac{\sum\left(\frac{x}{\sigma^2}\right)}{\sum\left(\frac{1}{\sigma^2}\right)} \tag{B.4}$$

For counting data (i.e. the number of scattered protons detected), the statistical error was assumed to be given by the following formula.

$$StatisticalError = \sqrt{N} \tag{B.5}$$

Finally, for a ratio of values, A/B, the error on the ratio was taken to be given by the following equation:

(B.6) $$\left(\frac{\sigma_{ratio}}{ratio}\right) = \sqrt{\left(\frac{\sigma_A}{A}\right)^2 + \left(\frac{\sigma_B}{B}\right.}$$

CALCULATION OF ERROR ON FC READINGS AND LEFT MASS SLIT

To determine the error on FC4 and FC1 readings, the ratio of the first 300s of elastically scattered protons to each FC reading was computed. Average values were calculated for each ratio, for each group of runs, as shown below.

Elastics (First 300s)/FC1 Analysis

1b. 'Good' R runs

Average Value:	11.64
Standard Deviation:	0.76
Percentage Error:	6.51

3. Postdsssd era blue runs

Average Value:	11.00
Standard Deviation:	0.61
Percentage Error:	5.57

Elastics (First 300s)/FC4 Analysis

1b. 'Good' R runs

Average Value:	6.08
Standard Deviation:	0.49
Percentage Error:	8.14

3. Postdsssd era blue runs

Average Value:	5.14
Standard Deviation:	0.28
Percentage Error:	5.48

Then, making the assumption that the error in the ratio depended on the error in the elastic proton integral and the error in the FC value according to equation B.6, and that the error in the elastic monitor integral was purely statistical according to equation B.5, the error in the FC values were calculated as shown below.

1/N (Counts in first 300s SB0 Peak)

1b. 'Good' R runs

Average Value:	0.000158
Standard Deviation:	0.000026
Percentage Error:	16.69
Standard Deviation of the Mean:	0.000003

3. Postdsssd era blue runs

Average Value:	0.00017
Standard Deviation:	0.00003
Percentage Error:	16.73
Standard Deviation of the Mean:	0.00001

Error in FC1 Value

1b. 'Good' R runs

Percentage Error :	6.39

3. Postdsssd era blue runs

Percentage Error :	5.42

Error in FC4 Value

1b. 'Good' R runs

Percentage Error :	8.05

3. Postdsssd era blue runs

Percentage Error :	5.33

Similarly, now knowing the error on the FC values, the error on individual left mass slit readings was determined by considering the ratio of FC4/Left Mass Slit as shown on the next page.

Average FC4/LeftMassSlit Analysis

1. 'Good' runs

Average Value:	0.607
Standard Deviation:	0.057
Percentage Error:	9.44
Standard Deviation of the Mean:	0.005

2. Predsssd era yellow runs

Average Value:	0.940
Standard Deviation:	0.238
Percentage Error:	25.35
Standard Deviation of the Mean:	0.069

3. Postdsssd era blue runs

Average Value:	0.667
Standard Deviation:	0.047
Percentage Error:	7.08
Standard Deviation of the Mean:	0.009

Error in FC4 Value

1b. 'Good' R runs

Percentage Error :	8.05

3. Postdsssd era blue runs

Percentage Error :	5.33

Error in Left Mass Slit Value

1. 'Good' runs

Percentage Error:	4.93

3. Postdsssd era blue runs

Percentage Error :	4.66

CALCULATION OF AVERAGE AND WEIGHTED AVERAGE R VALUES

R-Values --> Take average in EXCEL, and standard deviation

1b. 'Good' R runs

Average R:	1293.2
Standard Deviation:	111.3
Percentage Error:	8.61
Standard Deviation of the Mean:	14.9

3. Postdsssd era blue runs

Average R:	1498.1
Standard Deviation:	82.8
Percentage Error:	5.52
Standard Deviation of the Mean:	21.4

All runs with R Values

Average R:	1338.8
Standard Deviation:	135.7
Percentage Error:	10.13
Standard Deviation of the Mean:	16.0

R-Values --> Take weighted average in EXCEL, and error

1b. 'Good' R runs

Weighted Average R:	1275.5
Standard Deviation:	112.7
Percentage Error:	8.84
Standard Deviation of the Mean:	15.1

3. Postdsssd era blue runs

Weighted Average R:	1494.6
Standard Deviation:	83.5
Percentage Error:	5.58
Standard Deviation of the Mean:	21.5

All runs with R Values

Weighted Average R:	1341.5
Standard Deviation:	136.3
Percentage Error:	10.16
Standard Deviation of the Mean:	16.2